GL02342

PHILLIP M. WRIGHT

LBL-15526
UC-66b

Lawrence Berkeley Laboratory
UNIVERSITY OF CALIFORNIA

EARTH SCIENCES DIVISION

ELECTROMAGNETIC SOUNDINGS OVER A GEOTHERMAL RESERVOIR IN DIXIE VALLEY, NEVADA

M.J. Wilt and N.E. Goldstein

April 1983

Prepared for the U.S. Department of Energy under Contract DE-AC03-76SF00098

Printed in the United States of America
Available from
National Technical Information Service
U.S. Department of Commerce
5285 Port Royal Road
Springfield, VA 22161
Price Code: A04

LBL-15526

ELECTROMAGNETIC SOUNDINGS OVER A GEOTHERMAL RESERVOIR IN DIXIE VALLEY, NEVADA

M.J. Wilt and N.E. Goldstein

Earth Sciences Division
Lawrence Berkeley Laboratory
University of California
Berkeley, California 94720

April 1983

This work was supported by the Assistant Secretary for Conservation and Renewable Energy, Office of Renewable Technology, Division of Geothermal and Hydropower Technologies of the U.S. Department of Energy under Contract No. DE-AC03-76SF00098.

ELECTROMAGNETIC SOUNDINGS OVER A GEOTHERMAL RESERVOIR IN DIXIE VALLEY, NEVADA

ABSTRACT

An electromagnetic (EM) sounding survey was performed over a region encompassing the Dixie Valley geothermal field with the purpose of mapping the subsurface resistivity in the geothermal field and its surroundings. The EM survey consisted of 19 frequency-domain depth soundings made with the EM-60 system using three separate horizontal-loop transmitters, and was designed to explore a narrow region adjacent to the Stillwater Range to a depth of 2-3 km. Most sounding curves could be fitted to three-layer resistivity models. The surface layer is moderately conductive (10-15 ohm-m), has a maximum thickness of 500 m, and consists mainly of alluvial fan and lake sediments. More conductive zones are associated with hydrothermally altered rocks; a resistivity high may be associated with siliceous hot spring deposits. The conductive second layer (2-5 ohm-m) varies in thickness from 400 to 800 m and thickens toward the center of the valley. This layer probably consists of lacustrine sediments saturated with saline waters. Local resistivity lows observed in the second layer may be related to elevated subsurface temperatures. This layer may act as a cap rock for the geothermal system. Resistivities of the third layer are high (50-100 ohm-m) except in a narrow 5-km band paralleling the range front. This low-resistivity zone, within volcanic rocks, correlates well in depth and location with reported zones of geothermal fluid production. It also seems to correlate with the western margin of a concealed graben structure previously inferred from other geophysical data.

INTRODUCTION

During the summer of 1982, an electromagnetic sounding survey was made over a recently discovered geothermal field located in the northern part of Dixie Valley, Nevada; 19 electromagnetic soundings were obtained using the Lawrence Berkeley Laboratory EM-60 system (Morrison et al., 1978; Wilt et al., 1982). The soundings were designed to explore to a depth of 2 km over a zone adjacent to the Stillwater Range and encompassing the known geothermal field. The purpose of the survey was to help define the geothermal field boundaries and the possible structural controls on the geothermal system.

GEOLOGIC SETTING

Dixie Valley, a north-northeast-trending basin in central Nevada, is about 80 km long and 15 km wide at its widest point (Figure 1). The region is known for its high seismicity (Ryall and Vetter, 1982) and numerous active hot springs (Sass et al., 1971) and is thought to be a locus of crustal spreading in northern Nevada (Wallace, 1977). Regional geologic mapping has been done by Page (1965), Speed (1970), and Willden and Speed (1974). Regional geophysical studies, including passive and active seismics, gravity, and magnetics, are reported by Smith (1968), Thompson and Burke (1974), Wallace (1977), and Ryall and Vetter (1982).

Much of the lithologic information for rocks underlying Dixie Valley has been derived from exposures in the Stillwater Range (Figure 1). The range contains several deformed Mesozoic units (mainly sandstones, some volcanic breccias and conglomerates, thin limestones, tuffs, and volcanic flow interbeds) separated by thrust faults. The range is the center of a

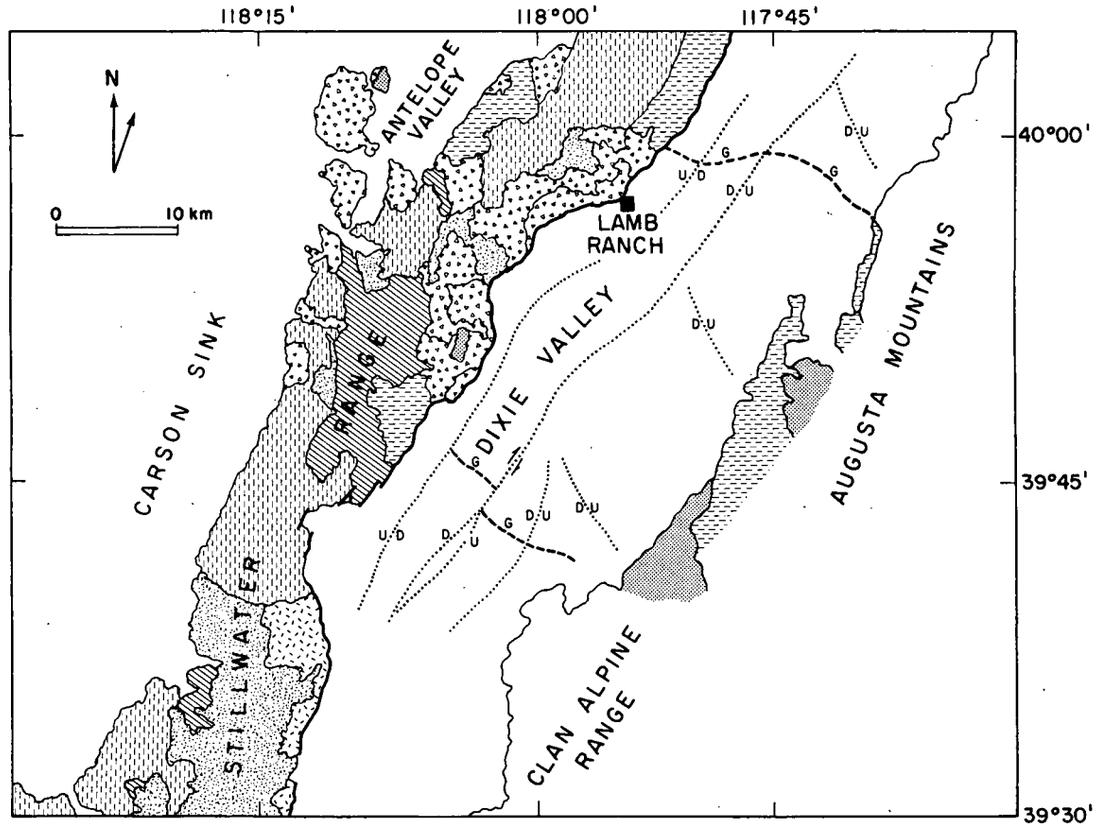

FAULT
SUBSURFACE GABBRO CONTACT
FAULT INFERRED FROM MAG.

TERTIARY - QUATERNARY	PLIO-PLEISTOCENE		BASALT AND BASALTIC ANDESITE
	PLIOCENE (?)		NON- MARINE SEDIMENTS AND TUFFS
	MIOCENE (?)		VOLCANIC TUFFS, BRECCIAS, AND FLOWS OF RHYOLITE, DACITE, LATITE, ANDESITE
TERTIARY AND MESOZOIC			PRE- LAHONTAN SEDIMENTS AND VOLCANICS
			GRANITE, QUARTZ, MONZONITE, GRANODIORITE
MESOZOIC	UPPER JURASSIC		BASALT FLOWS, TUFFS, AND BRECCIAS
			GABBROIC AND DIORITIC INTRUSIVES
	JURASSIC		METAVOLCANIC TUFFS, BRECCIAS, AND FLOWS
	UPPER TRIASSIC		LIMESTONE

HUMBOLDT LOPOLITH

XBL 833-1730

Figure 1. General geologic map of the Dixie Valley region.

large complex of mafic igneous rocks called the Humboldt gabbroic complex (Speed, 1970)--a lopolith 1 km thick that is composed chiefly of basaltic lavas and breccias but which grades downward into porphyritic and aphanitic mafic plugs, dikes, and sills (Willden and Speed, 1974).

The Stillwater Range is a horst bounded by normal faults with large vertical displacements; normal faults with smaller displacements cut across the axis of the block. The Stillwater Fault is the main fault system in the area. It bounds the Stillwater Range on the southeast and trends N36°E from Dixie Meadows, which is immediately south of the survey area, into Pleasant Valley, just north of the survey area.

Dixie Valley is situated to the east of the Stillwater Range and has been described as an eastward-tilted basin filled predominantly with Quaternary alluvium and lacustrine sediments (Smith, 1968; Speed, 1970). Photogeologic analysis (Whitney, 1980) indicates that the valley is a complex graben bounded by high-angle normal faults typical of the Basin and Range Province. The Tertiary section underlying the Quaternary valley fill is presumed similar to that observed in the adjacent Stillwater and Clan Alpine Ranges: mainly basalt and andesite flows and breccias, rhyolitic tuff, and associated sedimentary interbeds. The Tertiary section probably attains a maximum thickness of 1 km. Underlying the Tertiary rocks and crossing beneath the northern part of the Dixie Valley is the downfaulted extension of the Humboldt gabbroic lopolith. The subsurface position of this igneous intrusive has been determined by interpreting aeromagnetic data (Smith, 1968; Speed, 1970). Gravity and magnetic evidence in the northern part of Dixie Valley suggests a concealed north-northeast-trending central graben

(Smith, 1968). Gravity and magnetic data suggest that sediments attain a maximum thickness of 1.8 km within the graben.

Dixie Valley is one of the most tectonically active regions in the Great Basin. A magnitude 6.8 earthquake occurred in 1954 at Dixie Valley Hot Springs in Dixie Valley, and earthquakes of only slightly lesser magnitude have occurred within 100 miles in 1915, 1932, and again in 1954. Recent motion has created an almost continuous escarpment that is traceable along the Stillwater Range front for about 200 km. A 40-km segment of the range front fault in northern Dixie Valley, including the portion adjacent to the geothermal field, has been relatively quiet and has sustained no significant fault motion for several thousand years (Ryall and Vetter, 1982). A high level of microseismic activity is reported throughout Dixie Valley (Ryall and Vetter, 1982). Events occur almost exclusively along the steeply dipping Stillwater Range Fault. Motion on the fault is predominantly dip slip along a zone dipping 50-60° to the east. Focal depths are 10 km or more in southern Dixie Valley, decreasing to 7 km or less in the northern part of the valley.

There are a number of hot springs in northern Dixie Valley. The area near the geothermal field has at least three active hot springs, but none are within the survey area. Extensive zones of surface hydrothermal alteration are also evident along the western edge of Dixie Valley. A number of geothermal exploration wells have been drilled in the northern part of Dixie Valley, principally by Sunedco, Inc. It has been reported that the wells are 6000-8000 ft deep, with bottom-hole temperatures in excess of 450°F (Geothermal Hot Line, 1981). Most of the wells were completed in Tertiary

volcanics. As the wells were privately financed, detailed well data and log information have remained proprietary.

FIELD SURVEY

The locations of the three loop transmitters and the receiver stations for the EM survey are given in Figure 2. Transmitter-receiver separations ranged from 1 to 5 km, and data were collected in the frequency band from 0.05 to 200 Hz. This translates to a maximum depth of penetration of 2-3 km. Field data were collected in July 1982 under ideal access and weather conditions; 19 field soundings were taken in 5 days for an average rate of about 4 soundings per day.

EM sounding data were reduced on site using an in-field computer, although some post-field processing was neccessary before quantitative interpretation could be done. The in-field processing capability proved very useful for evaluating data quality on site. Interpretation was done primarily in the laboratory, although apparent resistivity spectra were calculated and displayed in the field for preliminary evaluation.

Appendix A gives a detailed description of the EM-60 system and the procedures used in collecting and interpreting data.

RESULTS AND INTERPRETATION

One-dimensional (layered-model) interpretation was performed on all Dixie Valley EM soundings. Model parameters were obtained by automatic inversion; final parameters and field plots are given in Appendix B. For most stations, only ellipse polarization spectra were used for the inversions.

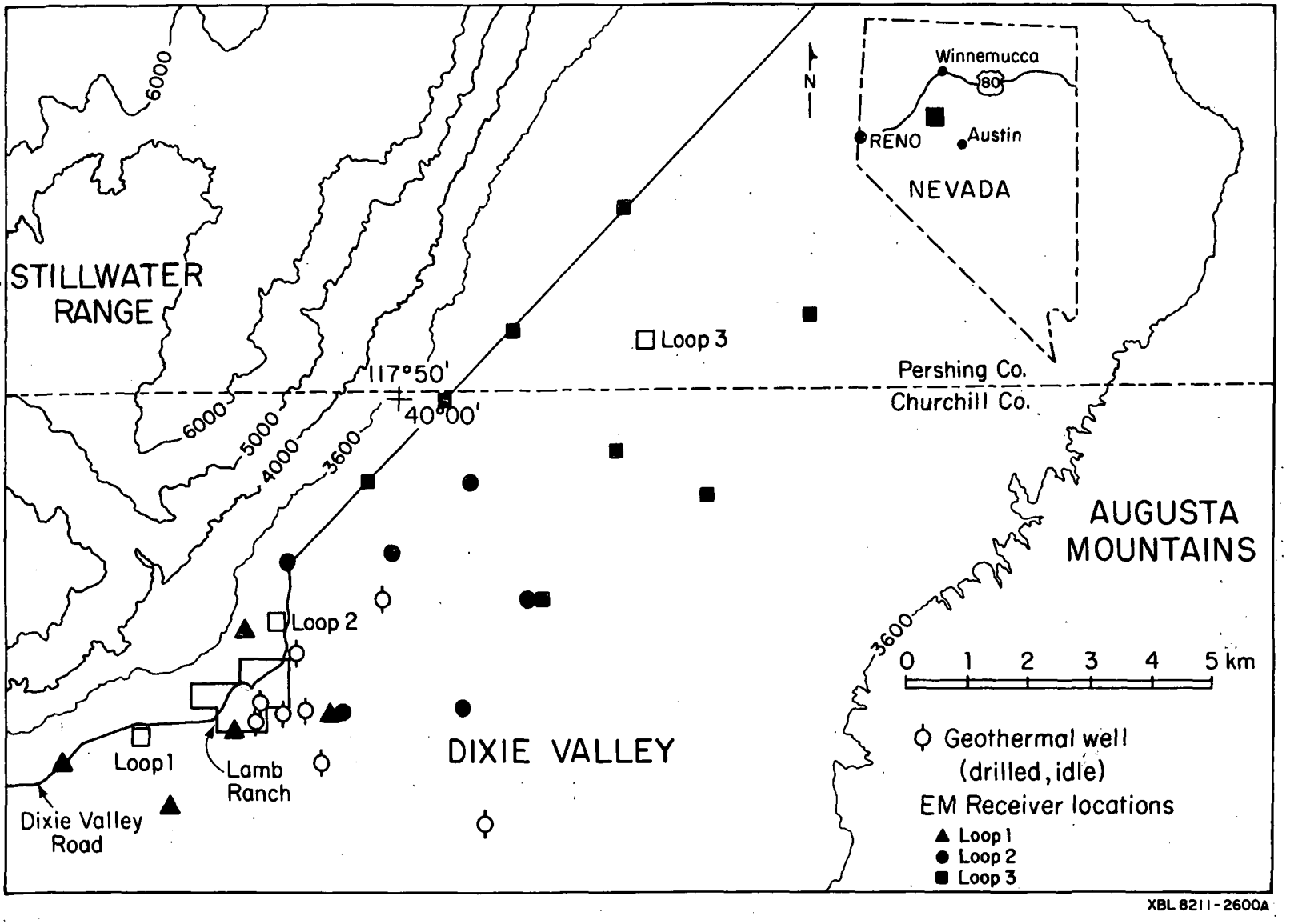

Figure 2. Transmitter-receiver locations for EM-60 survey in Dixie Valley.

That is, the ellipticity and tilt-angle spectra were defined by the combined vertical and radial magnetic fields. This technique has the advantage of not requiring absolute phase and amplitude spectra of the magnetic fields; only the relative phases and amplitudes are used. The calculations are therefore insensitive to such errors as clock drift and miscalibration of amplifiers or filters, and much less sensitive to sensor misalignment than absolute phase data. When parts of the magnetic field spectra for one channel were missing or noisy, absolute phases and amplitudes from the good channel were used.

A three-layer starting model, obtained from a simple inversion of apparent resistivity plots, was taken as a first guess for the inversions. The starting model had a surface layer of resistivity 20 ohm-m and thickness 200 m, a middle layer of resistivity 5 ohm-m and thickness 500 m, and a basal layer of resistivity 100 ohm-m and infinite thickness. The surface layer represents undersaturated and freshwater-saturated alluvium and other unconsolidated sediments. The second layer represents older alluvial and lacustrine deposits saturated with brackish pore water. This layer represents sediments analogous to the present-day Humboldt Salt Marsh Playa deposits. The basal layer is probably made up of Tertiary volcanics underlain by Mesozoic gabbros and metasediments. Most field soundings could be fitted to this type section, although the individual layer parameters varied greatly from sounding to sounding. For several soundings, a two-layer model was more appropriate; the soundings were either too close to the transmitter to penetrate to the bottom layer or too far from the transmitter to resolve the top layer. For other soundings, particularly those taken within the geo-

thermal field, the basal layer was less resistive. A good fit was achieved between observed and calculated field values at all sounding locations.

In Figures 3 to 7, layer-model parameters are contoured for the three-layer section; parameter values are plotted at a location halfway between the transmitter and the receiver. Maps are presented of the individual layer resistivities for the three-layer section and the thicknesses of the upper and middle layers. The figures give an areal view of the variation of subsurface parameters; they can provide insight to the subsurface resistivity structure.

Figure 3 shows the resistivity of the upper layer. The resistivity ranges from 7 ohm-m for a sounding taken at the south end of the survey area to 50 ohm-m for one taken near the Lamb Ranch. The average resistivity is 10-15 ohm-m, which is a reasonable value for young, freshwater-saturated sediments. The thickness of the upper layer (Figure 4) ranges from 0.14 to more than 0.6 km. It is thinnest near the Stillwater Range front and thickest at stations located to the north and in the center of the valley. For some of these northern stations, the transmitter-receiver separations were more than 3 km. At these large separations, surface layers tend to be lumped together, so that this layer may represent a sum of two or more thinner layers. At several places along the Stillwater Range front, hydrothermal alteration is evident. Alteration correlates well with places where the surface resistivity is less than 10 ohm-m. There is also a low-resistivity anomaly near the Lamb Ranch that may be related to near-surface leakage of geothermal fluids. The zone of high near-surface resistivity west of the Lamb Ranch is unusually high for alluvial sediments and may

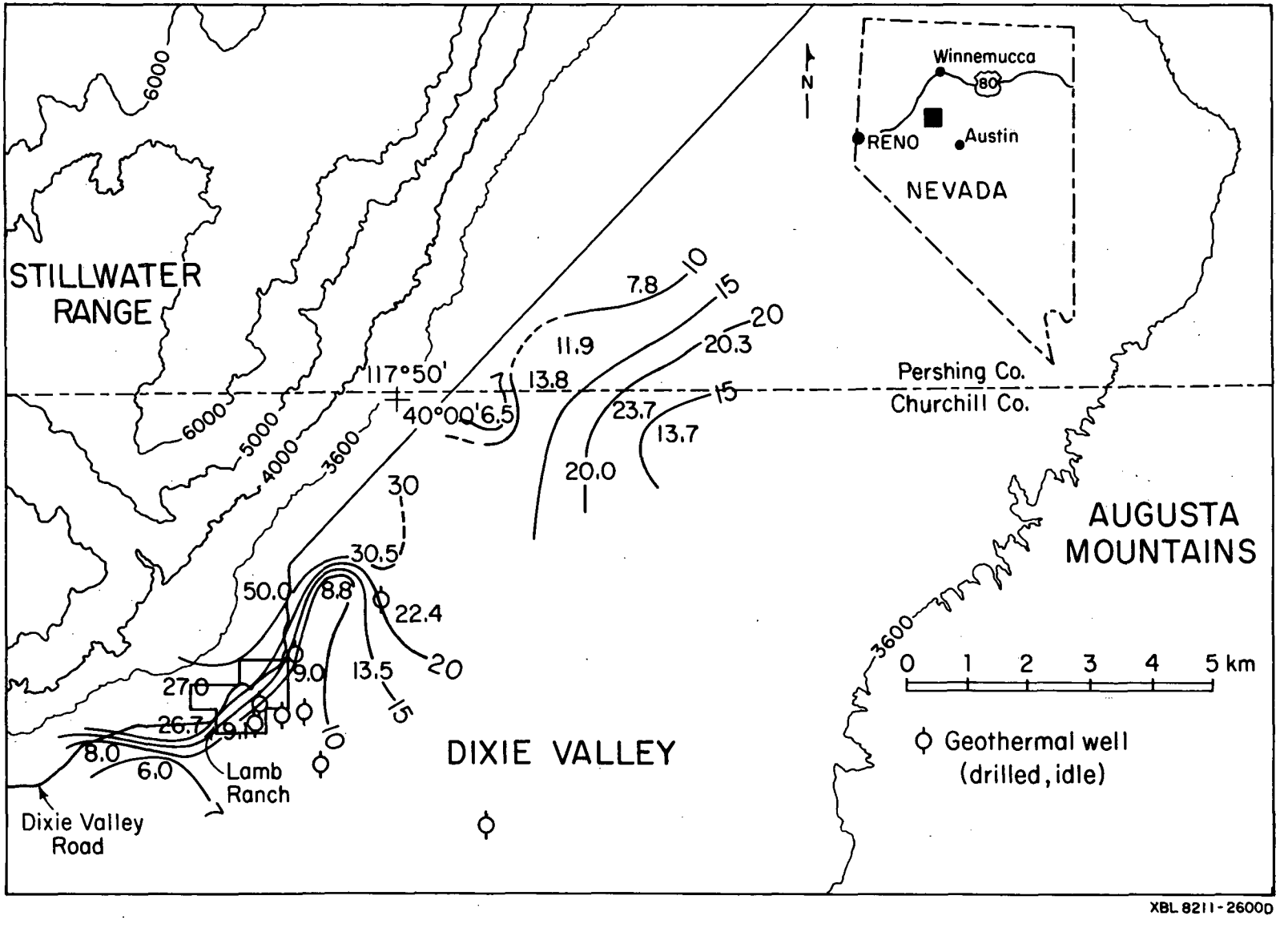

Figure 3. Resistivity of the upper layer (ohm-m).

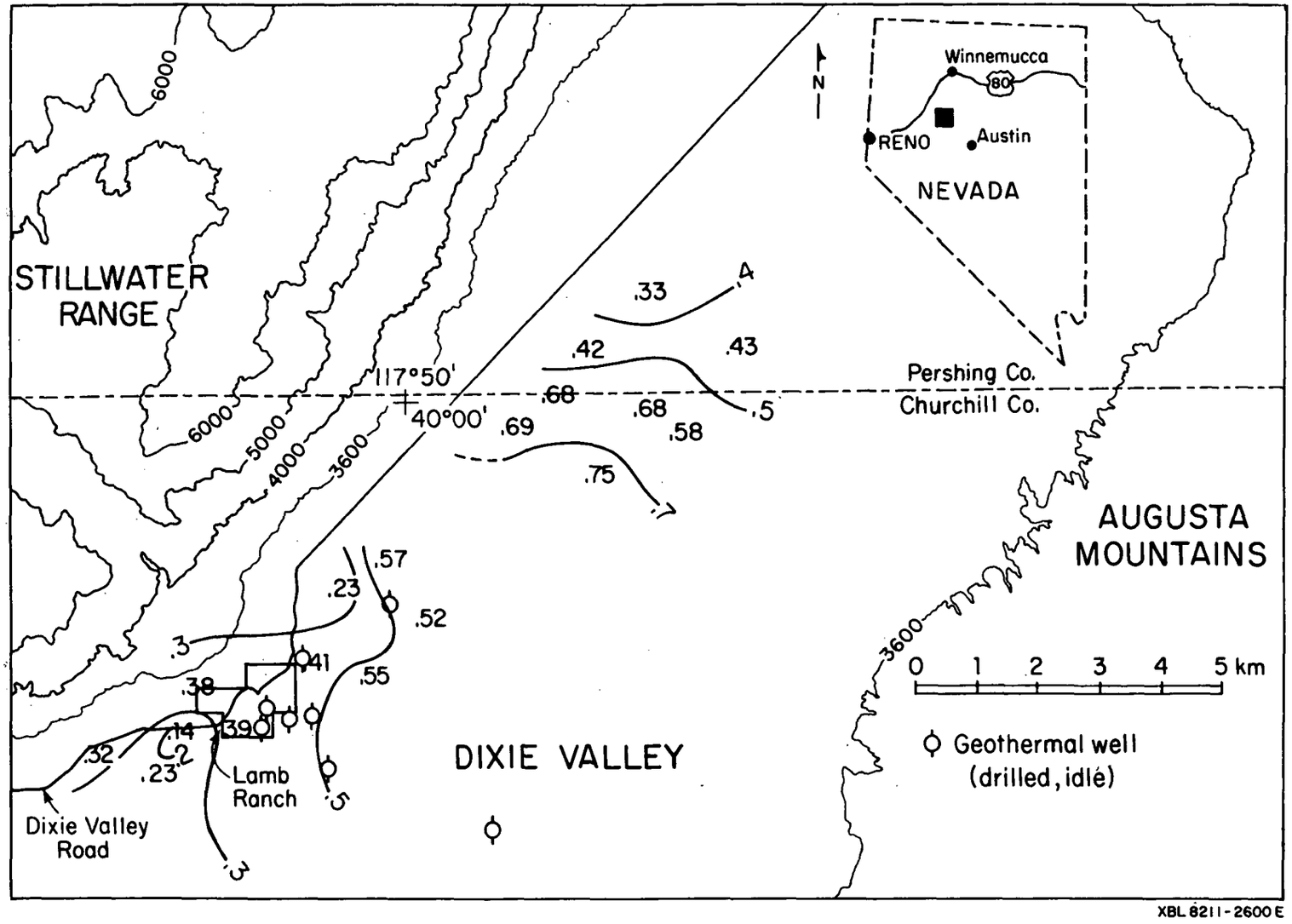

Figure 4. Thickness of the upper layer (km).

represent silicified sinter deposits associated with former hot spring activity. The upper layer shows general overall decrease in resistivity from north to south. This corresponds to a drop in elevation toward low-lying regions in the southern part of the survey area, so that this trend probably follows subsurface water flow and is also probably related to an increase in clay content of sediments and an increase in groundwater salinity.

Figure 4 shows the resistivity of the middle layer; Figure 5 shows the cummulative thickness of the upper and middle layers. Resistivity of the middle layer varies from 1.5 to 5 ohm-m. The lowest values are near the known geothermal field in the Lamb Ranch area and adjacent to the Stillwater Range front in the northern survey area. In both cases the primary cause for the low resistivity may be elevated temperatures due to nearby geothermal waters. The cumulative thickness of the upper and middle layers (or depth to the basal layer) varies considerably over the area surveyed (Figure 5). Contours show a steep dropoff in the depth to the basal layer from the Stillwater Range eastward into the valley. The depths increase from about 400-600 m to 1.5 km or more over a distance of less than 2 km. The steep dropoff aligns well with the interbasin graben proposed by Smith (1968) and Wallace (1977). The depth of the basal layer corresponds well in some areas to gravity and magnetic interpretations but poorly in the known geothermal field, indicating that the basal layer does not always represent basement rock or that bedrock is locally fractured. The western edge zone of steep dropoff trends roughly parallel to the range front throughout the survey area. It may represent the basinward extension of the range front faulting.

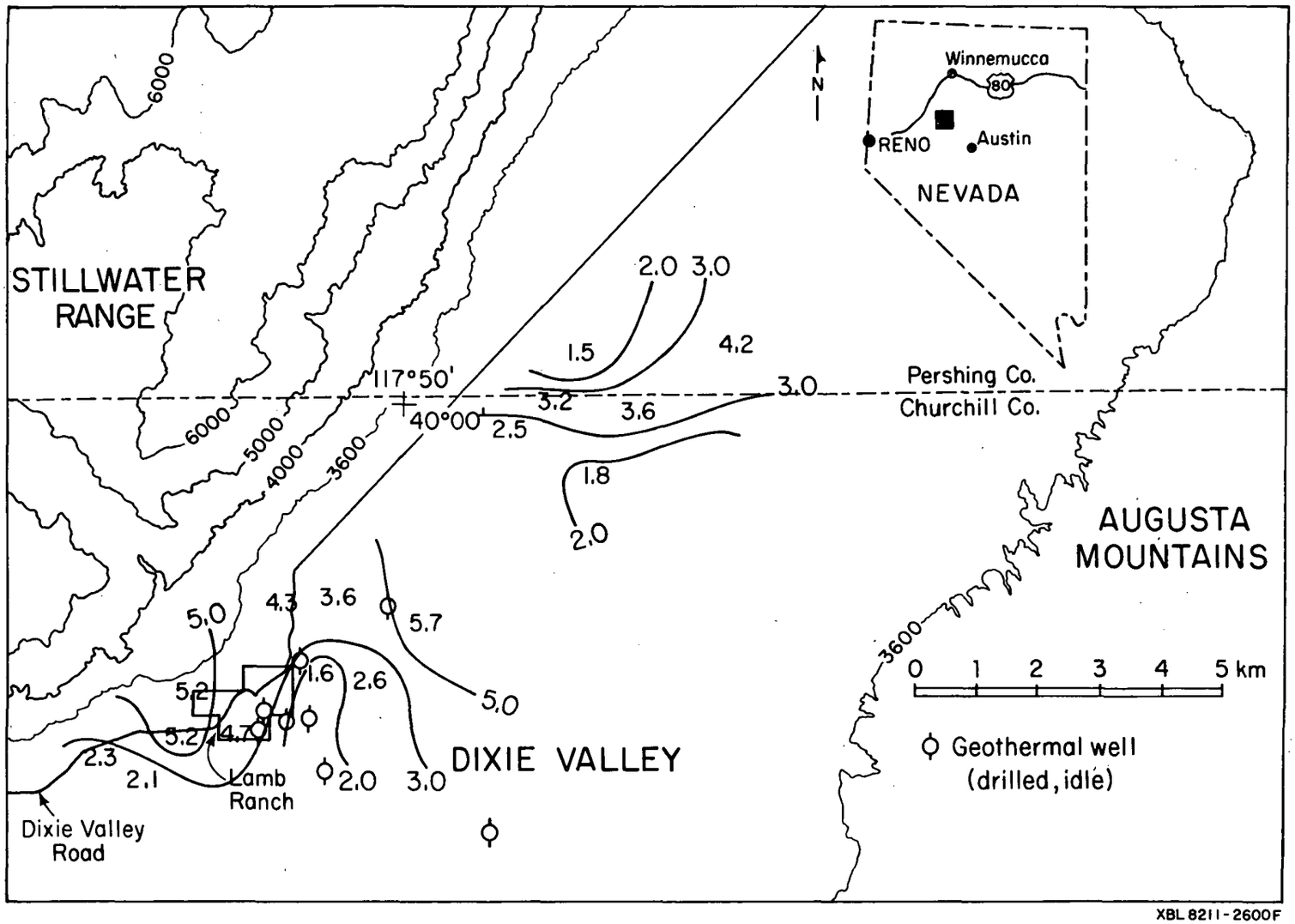

Figure 5. Resistivity of the middle layer (ohm-m).

As no soundings were made on the eastern side of the valley, the character of the eastern margin of the graben was not investigated.

Figure 6 shows the resistivity of the basal layer. This map indicates a narrow, elongated region of low resistivity in the basal layer stretching from the Lamb Ranch northward along the Stillwater Range front for almost 5 km. Resistivities in this anomalous zone range from 2 to 50 ohm-m. Outside this belt the basal layer is more resistive. The EM soundings do not resolve the actual resistivity well because the layer contributes little to the measured response; for many soundings the resistivity of the basal layer was therefore considered to be 100 ohm-m. The top of the low-resistivity zone is 1-1.5 km deep, but the thickness of this zone was not determined. The low-resistivity belt correlates well in location and depth with the occurrence of deep geothermal fluid encountered in the Sunedco wells near the Lamb Ranch. Figures 6 and 7 show that the low-resistivity region also correlates with the western margin of the graben described by Smith (1968) and Speed (1970), hence it is likely that the graben faults are important in providing fluid conduits and permeability for the system. The existence of a thick, clay-rich middle layer may provide a sealing cap for the system.

CONCLUSIONS

Electromagnetic sounding measurements were successful in mapping the subsurface resistivity distribution in the northern part of Dixie Valley to a depth of about 2 km. A three-layer model was used, where the upper layer represents alluvial sediments; the middle layer, lacustrine deposits; and the basal layer, Tertiary and older rocks. Variations in resistivity and

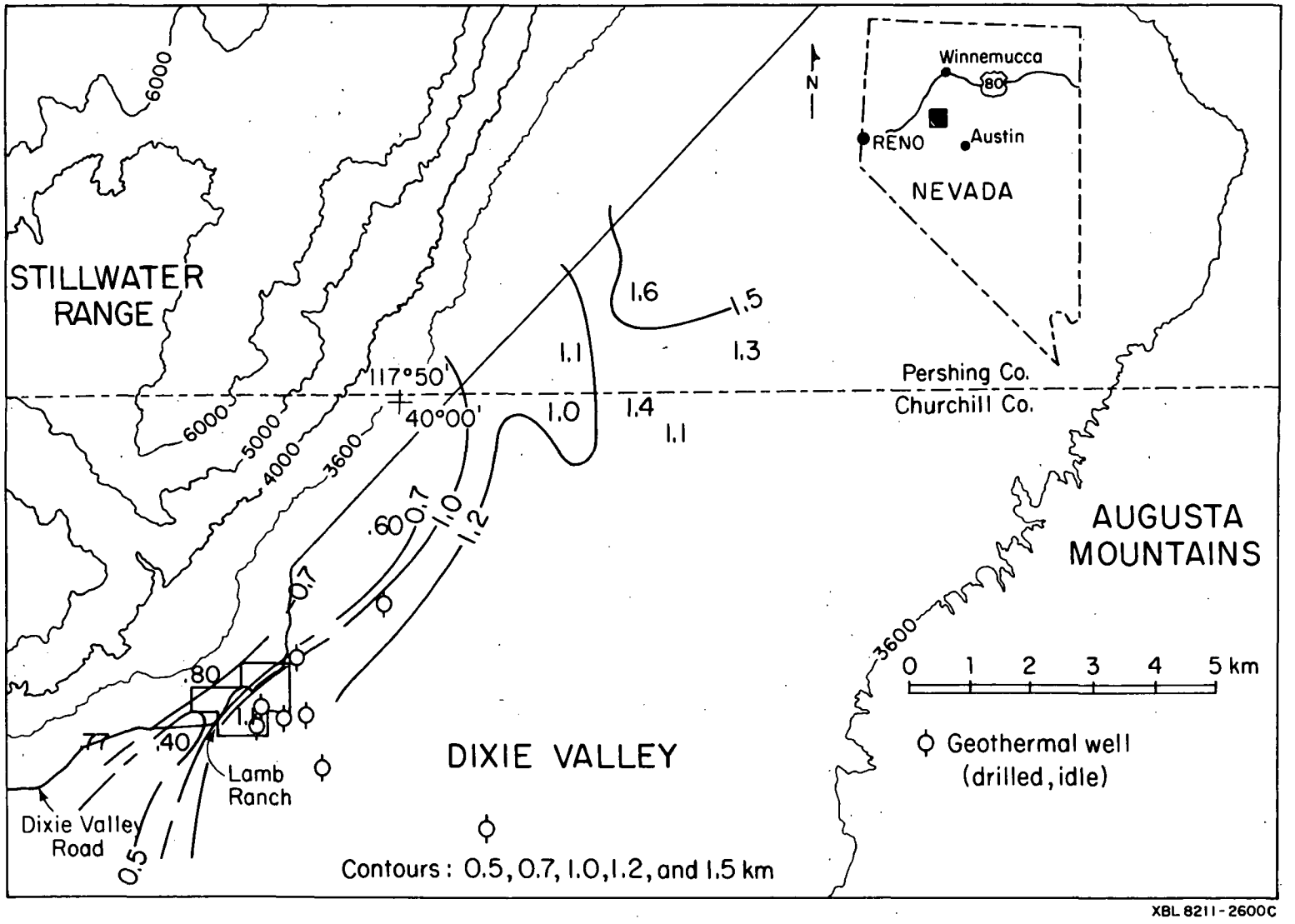

Figure 6. Thickness of the upper and middle layers (km).

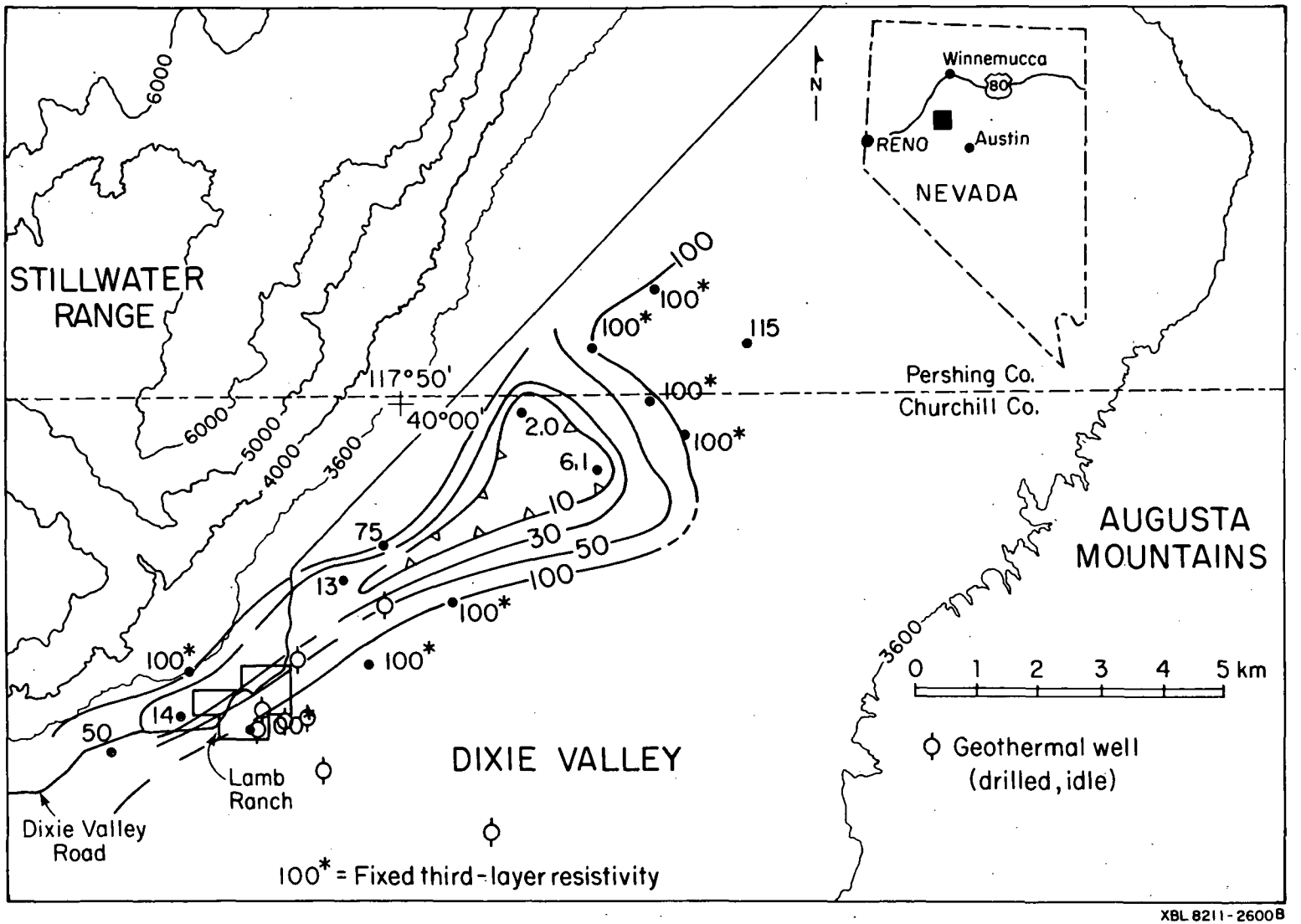

Figure 7. Resistivity of the basal layer (ohm-m).

thickness of these basic model parameters provided detail of structure and stratigraphy.

A deep low-resistivity anomaly is associated with the known geothermal field but extends several kilometers to the north, outside of known field boundaries. Depth to the resistivity low is consistent with geothermal fluid production depths. The lower boundary to the low-resistivity zone could not be determined.

The EM interpretation shows significant normal faulting within the basin of the western margin. These normal faults may play a major role in providing permeability and fluid conduits for the geothermal system.

ACKNOWLEDGEMENTS

We gratefully acknowledge the contributions of Don Lippert, Warren Harnden, and Ruben Zelwer for their assistance in the field work. We would also like to thank Mr. and Mrs. Sheldon Lamb for their warm hospitality during our field survey.

This project was supported by the Assistant Secretary for Conservation and Renewable Energy, Office of Renewable Technology, Division of Geothermal and Hydropower Technologies of the U.S. Department of Energy under Contract No. DE-AC03-76SF00098.

REFERENCES

Geothermal Hot Line, 1981, Dixie Valley well tested: Geothermal Hot Line, v. 11, no. 2, p. 54.

Morrison, H.F., Goldstein, N.E., Hoversten, M., Oppliger, G., and Riveros, C., 1978, Description, field test and data analysis of controlled source EM system (EM-60): Lawrence Berkeley Laboratory, LBL-7088.

Page, B.M., 1965, Preliminary geologic map of a part of the Stillwater Range, Churchill County, Nevada: Nevada Bur. Mines, Map 28.

Ryall, A.S., and Vetter, U.R., 1982, Seismicity related to geothermal development in Dixie Valley, Nevada: Seismological Laboratory, Univ. Nevada, Reno, DOE publication, DOE/NV/10054-3, 102 p.

Sass, J.H., Lachenbruch, A.H., Monroe, R.J., Greene, G.W., and Moses, T.J., 1971, Heat flow in the western United States: J. Geophys. Res., v. 76, p. 6376-6413.

Smith, T.E., 1968, Aeromagnetic measurements in Dixie Valley, Nevada; Implication on Basin-Range structure: J. Geophys. Res., v. 73, p. 1321-1331.

Speed, R.C., 1970, Geologic map of the Humboldt lopolith and surrounding terrain, Nevada: Geol. Soc. Am., Map MC-14.

Thompson, G.A., and Burke, D.B., 1974, Regional geophysics of the Basin and Range Province: Annual Review of Earth and Planetary Sciences, v. 2, p. 213-238.

Wallace, R.E., 1977, Patterns of faulting and seismic gaps in the Great Basin Province: U.S. Geol. Survey open-file report 78-943, p. 857-868.

Whitney, R.A., 1980, Structural-tectonic analysis of Northern Dixie Valley: Univ. Nevada, M.S. thesis, 65 p.

Willden, R., and Speed, R.C., 1974, Geology and mineral deposits of Churchill County, Nevada: Nevada Bur. Mines Geol., Bull. 83, 95 p.

Wilt, M.J., Goldstein, N.E., Stark, M., Haught, J.R., and Morrison, H.F., 1981, Experience with the EM-60 electromagnetic system for geothermal exploration in Nevada: Lawrence Berkeley Laboratory, LBL-12618.

APPENDIX A

EM-60 ELECTROMAGNETIC SYSTEM

With the EM-60 system, the earth is energized by means of an alternating magnetic field created by a square-wave current applied to a horizontal loop (Figure A-1). Power is provided by a Hercules gasoline engine linked to a 60-kw, 400-Hz aircraft alternator; the two components are mounted on the bed of a 1-ton four-wheel-drive truck. The alternator output is full-wave rectified and capable of providing $\pm$ 250 V at up to 400 A to the loop, although in practice we have never approached this current. The current waveform is created with a transistorized switch that consists of two parallel arrays of 6-60 transistors mounted in sets of three in interchangeable modules (Morrison et al., 1978). The operator remotely sets the fundamental frequency of the current waveform; four frequencies per decade are switch selectable. The fundamental frequencies are generated by means of a crystal-controlled oscillator over the range 10^{-3}-10^{3} Hz.

SYSTEM DESCRIPTION

The dipole moment, which is a measure of the primary field strength, is a function of the resistance and inductance of the loop. At frequencies below about 50 Hz a four-turn, 200-m square loop of 6-gauge wire will yield a dipole moment of 5×10^{6} mks. Except in very conductive terrain this provides adequate signal for transmitter-receiver separations less than about 4 km. Above 50 Hz the loop inductance reduces the moment and causes the current waveform to become quasi-sinusoidal. Because of the reduced moment, high-frequency information becomes more difficult to obtain at larger transmitter-receiver separations. The 200-m loop has proved satis-

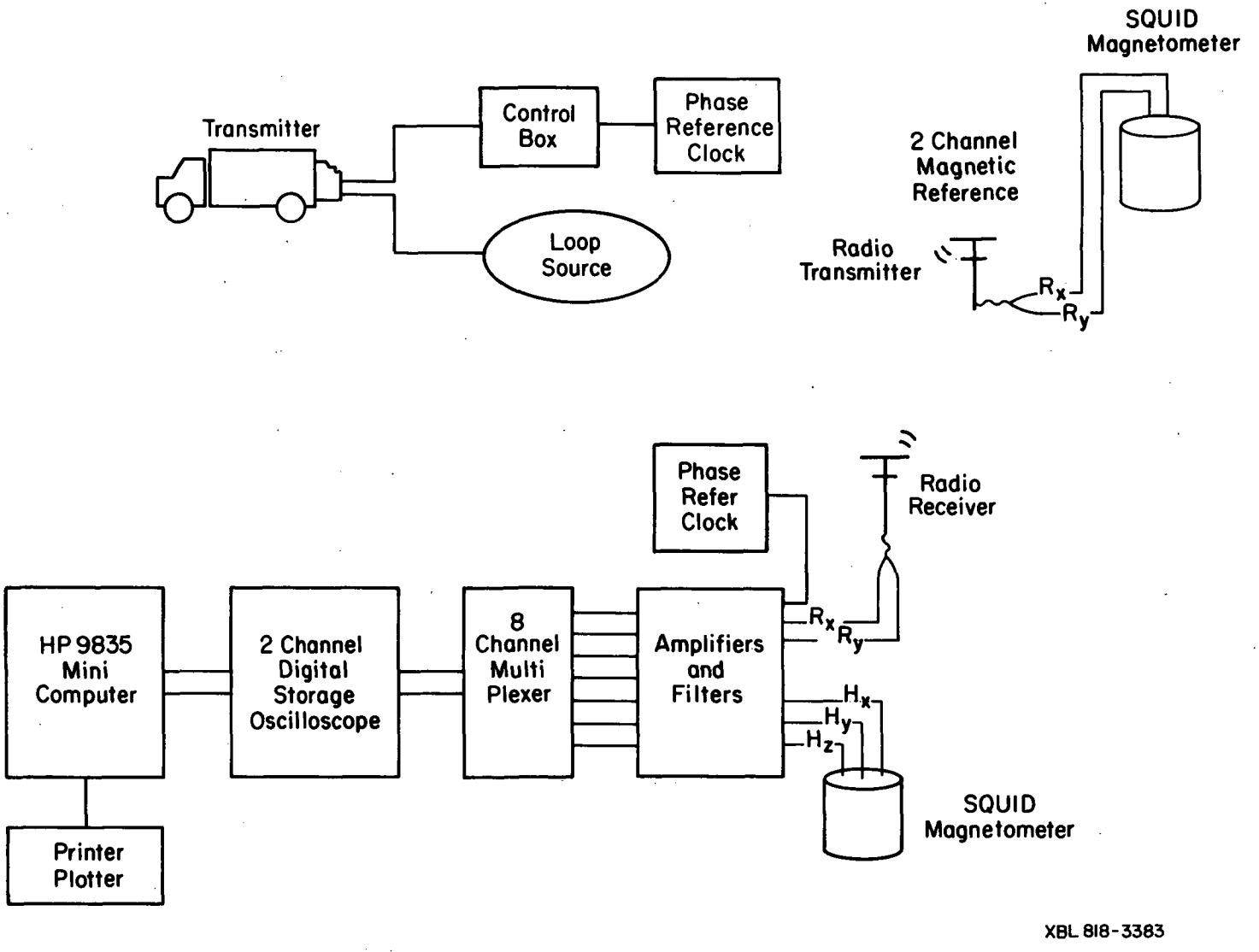

Figure A-1. Schematic diagram of the horizontal-loop EM-60 system.

factory for most geothermal operations: it can be laid out from a truck in about 30 minutes, and it provides sufficient power for exploration depths of up to 3 km. If greater depth of penetration is required, larger loops and/or heavier gauge wire can be used. However, to achieve a two-fold increase of exploration depth, an approximate four-fold increase in source strength is required, hence logistical problems associated with the greater weight and length of wire must be considered.

Magnetic fields were detected at receiver sites with a three-component SQUID magnetometer oriented to measure the vertical, radial, and tangential components with respect to the loop. Electric dipoles may also be used in combination with or instead of magnetic sensors.

The eight-channel system permits the measurement of two independent receiver sites in addition to a reference magnetometer for noise cancellation. One of the two receiving sites, as well as the reference magnetometer, transmits signals to the receiver van via FM telemetry. All signals are amplified and filtered prior to processing; both anti-alias and notch filters are used. After analog treatment the signals are multiplexed into two data lines and then input to a two-channel Nicholet digital oscilloscope. The oscilloscope digitizes, buffer-stores, and displays signals before digital processing with an in-field computer. All subsequent calculations and plots are performed on a Hewlett Packard HP9835 computer. Fourier transformation is accomplished with a fast assembler code, and the remaining calculations are programmed in Basic computer language.

Processing results in an amplitude and phase estimate of all magnetic fields. Amplitudes are normalized by the free-space primary field from the

transmitter. Phase referencing is maintained by highly accurate quartz clocks. The computer also calculates ellipse polarization parameters (the ellipse traced by the combined magnetic fields), ellipticity and tilt angle, and apparent resistivity. Ellipse polarization parameters provide useful data for layered-model interpretations; apparent resistivity is valuable for in-field interpretation and data quality evaluation. The computer also calculates confidence limits on data and provides spectral plots of all data.

At low frequencies ($f < 1.0$ Hz), natural geomagnetic signal amplitude increases roughly as $1/f$, and the secondary (induced) magnetic field decreases as $1/f$. The net result is an effective signal-to-noise ratio that decreases as $1/f^2$. High levels of geomagnetic noise can therefore be a formidable barrier to obtaining low-frequency information, particularly on the horizontal component channels. To reduce the effect of geomagnetic noise, a second (reference) magnetometer is placed at a convenient location far enough from the transmitter loop (usually about 10 km) that the observed remote fields consist only of the geomagnetic fluctuations (Figure A-2). Placed at a properly chosen site, the reference magnetometer need not be relocated during the course of a survey. The horizontal magnetic fields R_x and R_y at the remote site are transmitted to the mobile receiver station via FM radio telemetry. Before the loop is energized, the remote signals are inverted, adjusted in amplitude, and then added by scalar addition to the receiver station geomagnetic signal to produce essentially a null signal. Once the loop is energized, the resulting magnetic signals processed are virtually free of geomagnetic noise. A graphic illustration of the results of this simple noise cancellation scheme is shown in Figure A-2. The resulting signal-to-noise improvement of roughly 20 dB has allowed acquisition of

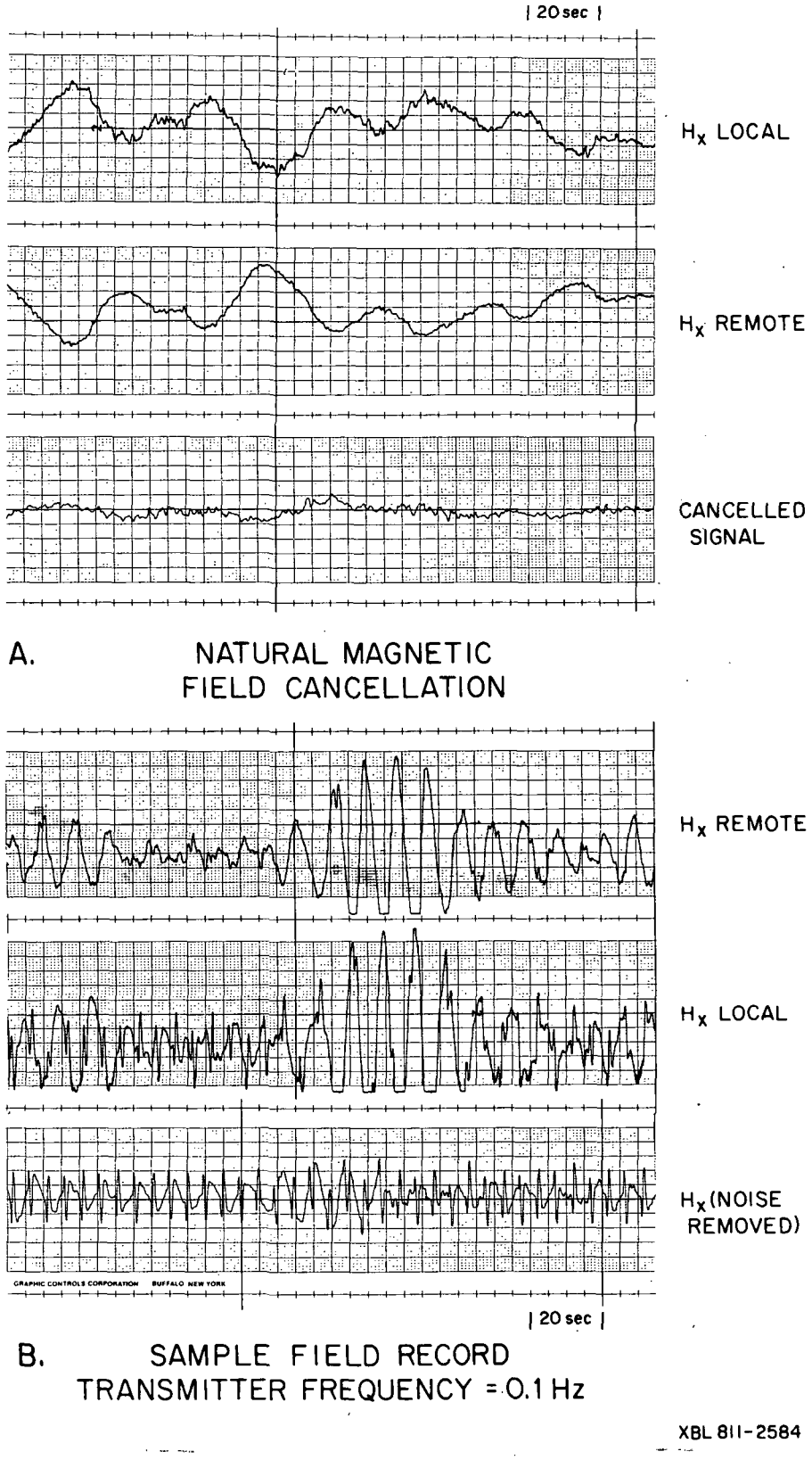

Figure A-2. Example of data improvement using the telluric noise cancellation scheme. (A) Natural geomagnetic signal and initial cancelling at the receiver site with transmitter off. (B) Same system with transmitter on.

data reliable to 0.05 Hz, an addition of three or four important data points on the sounding curve. These points are of great value for resolving deeper horizons. This noise cancellation scheme has reduced low-frequency averaging times by a factor of 4 and has allowed us to obtain low-frequency information even at high geomagnetic noise levels.

DATA INTERPRETATION

Apparent Resistivity Function

Apparent resistivity vs frequency curves can be calculated from EM spectra by matching observed field data to generalized, homogeneous half-space curves (Wilt and Stark, 1982). The generalized curves are a plot of spectral field value vs induction number (B), which is a function of the frequency, transmitter-receiver separation, and resistivity of the half-space. A resistivity spectrum can therefore be obtained by matching observed data to the generalized curve and calculating the conductivity from the induction number. For a multilayered section, an apparent resistivity curve is obtained from this calculation.

An example of such a curve calculated from a three-layer model is given in Figure A-3; calculations for each type of measured data reflect the layered-model section shown at the bottom, although there is scatter between the curves. The curves are generally used for qualitative interpretation. They give asymptotic values for earth resistivities and indicate the resistivity type section, thus allowing more accurate "first guesses" for the layered-model inversion algorithm. The curves are also useful for evaluating data quality in the field and for isolating noisy data for deletion prior to inversion.

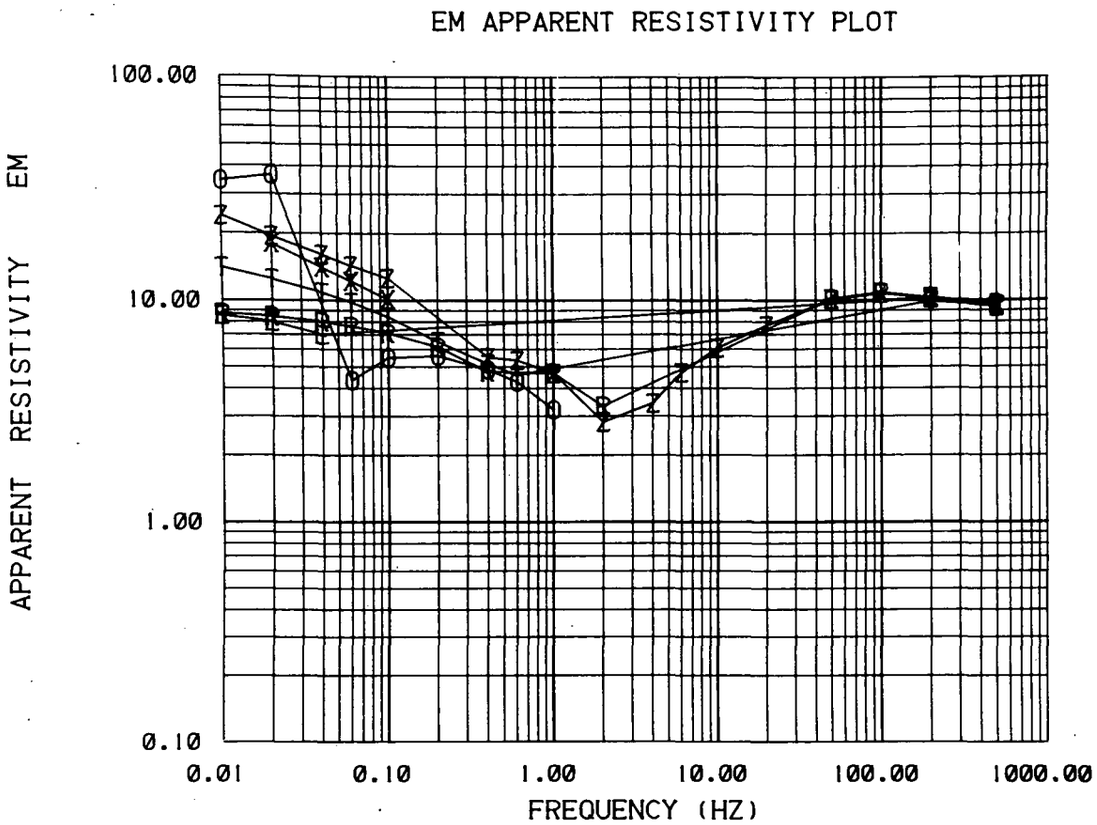

Figure A-3. EM apparent resistivity spectra calculated from layered-model theoretical data.

Layered-Model Inversion

Quantitative interpretation is accomplished by least-squares inversion of observed data to fit one-dimensional models. Layered-model forward solutions may be calculated for a finite-loop source or for a point dipole source (Ryu et al., 1970; Anderson, 1979). The loop-source solution is perfectly general and is more accurate when soundings are made close to the source. The point-dipole solution is calculated using digital filters and is identical to the loop solution for transmitter-receiver separations greater than 10 loop radii. Since the digital filter calculation is much less expensive, the point-dipole source is normally used in the layered-model inversion program. The inversion program uses the Marquardt least-squares algorithm to fit amplitude-phase and/or ellipse polarization parameters jointly or separately to layered models (Inman, 1975). This program allows the use of polarization parameters to fit the high-frequency points where absolute phase data is noisier and to use absolute phase data simultaneously to fit the lower frequencies, where the phase reference allows for better parameter resolution. Observed data are weighted by the calculated error of field measurements. Our experience indicates that one-dimensional interpretation seems to provide adequate results. Because of the rapid fall off in field strength with distance, dipole fields seem to be much less affected by nearby lateral discontinuities and current channeling, which, for example, impair one-dimensional magnetotelluric interpretations. Although we rely mainly on one-dimensional interpretations, two-dimensional forward modeling of dipole EM data may be done for special cases (Lee, 1978). The finite element program used for two-dimensional calculations is very expensive and cumbersome, however, and the model considered must be fairly simple to yield

an accurate solution. The program is used chiefly for theoretical studies, although it has been used occasionally to help interpret field data affected by severe two- or three-dimensional geology.

An example of a layered-model inversion for an EM-60 sounding is given in Figures A-4 and A-5. The vertical and radial amplitude and ellipticity spectra shown are three of the six spectra normally calculated for a field sounding, the others being vertical and radial phase and tilt angle. The data were fitted jointly to the two-layer model shown at the bottom of each figure.

In areas of rugged terrain it may be necessary to lay out the transmitter loop on an inclined surface. For this condition the source dipole must be treated as the sum of a vertical and a horizontal dipole, rather than the purely vertical dipole that is considered in the idealized, flat-earth case. To interpret field data properly for an inclined dipole, Haught et al. (1981) developed a computer program to calculate EM fields over a layered earth from an arbitrarily oriented dipole. The program combines layered-model solutions for vertical and horizontal dipoles at the appropriate strength and orientation to calculate the correct magnetic fields at the receiver sites. The solution was used in a least-squares inversion routine, and trials of the program provided good results at a reasonable cost.

An example of the effect of the tilted dipole is given in Figure A-6, which shows two interpretations for a set of EM sounding data obtained at the McCoy field area from a tilted dipole. The upper graph shows our attempt to interpret the data, assuming a vertical dipole. Of the various

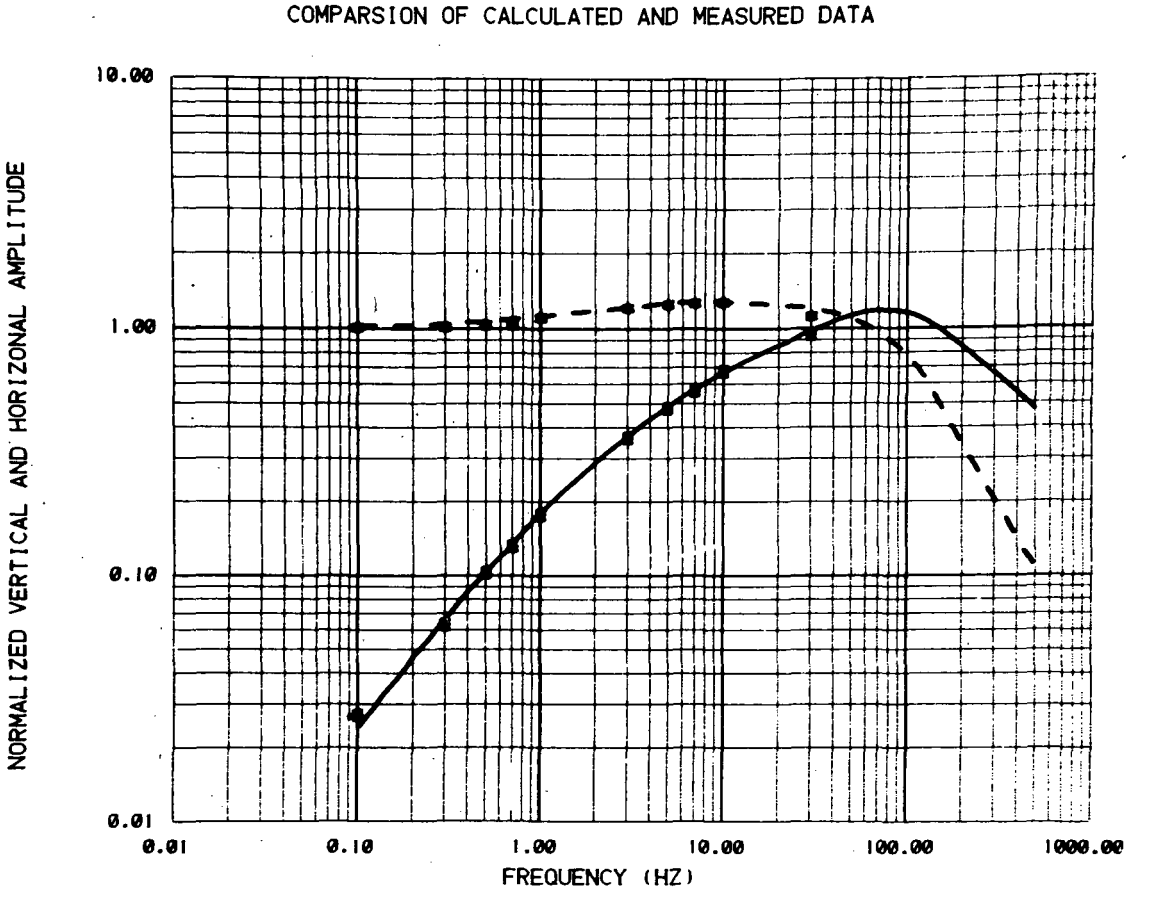

Figure A-4. Examples of the EM-60 vertical and horizontal amplitude spectra and their fit to a two-layer model.

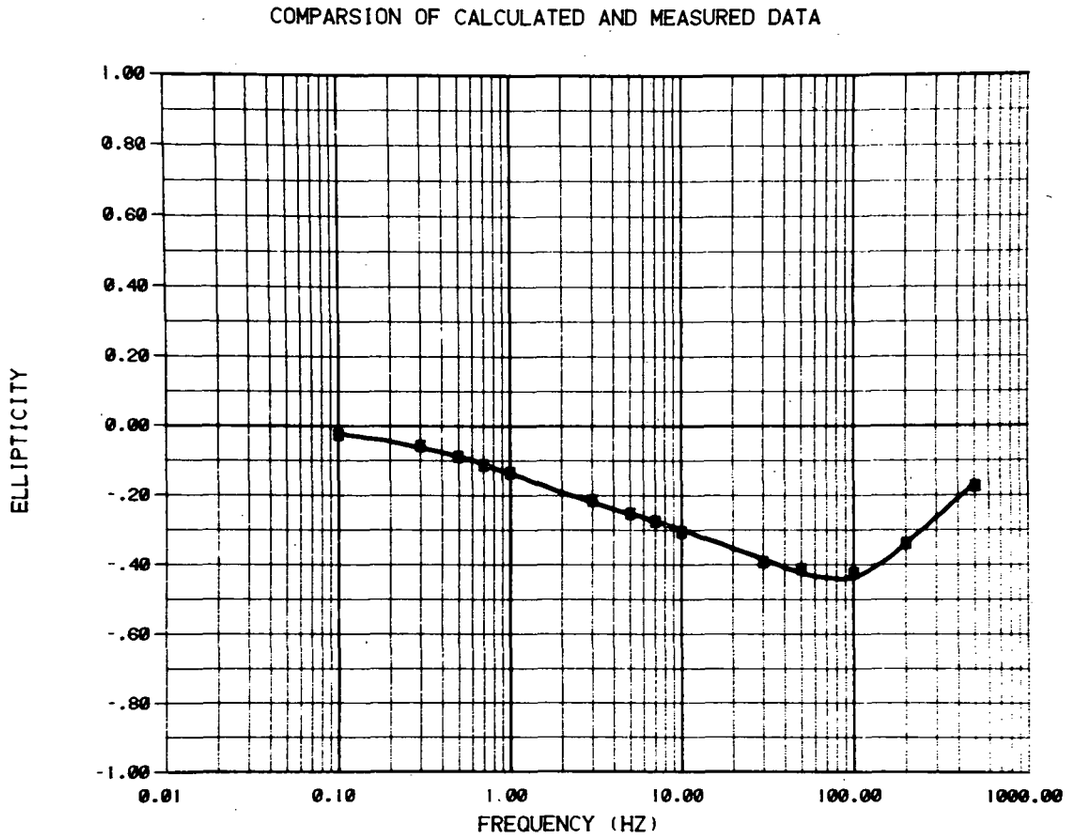

Figure A-5. Example of an EM-60 ellipticity spectrum and its fit to a two-layer model.

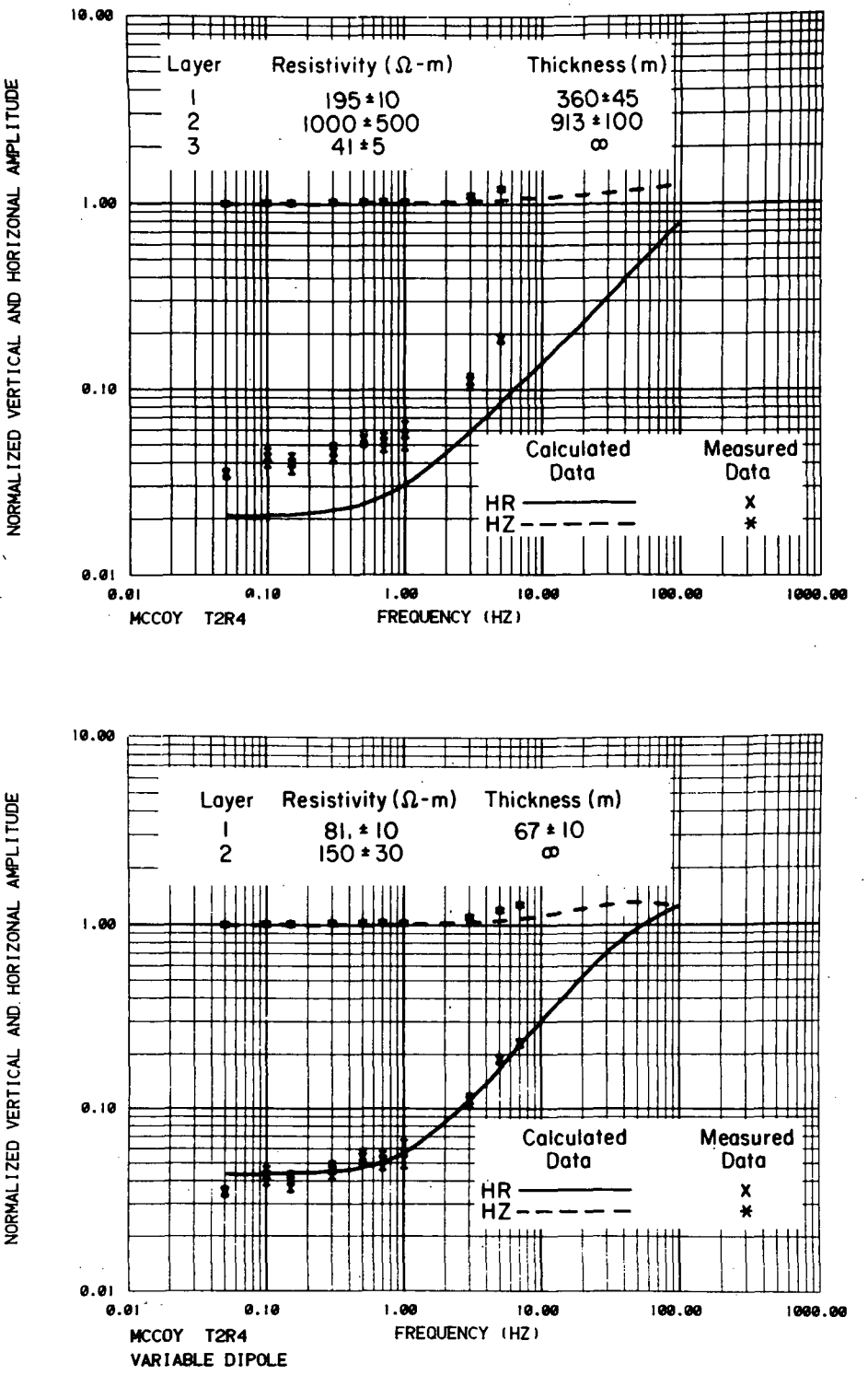

XBL 812-2617

Figure A-6. Comparison of inversions from a vertical dipole source (top) and a variable dipole source (bottom).

two- or three-layer models that we considered, the one that gives the best fit is a three-layer section that indicates the presence of a conductor at about 1.3 km in depth. The bottom of Figure A-6 shows a layered-model fit for a two-layer section with a tilted dipole source. Here the fit is superior, and with no indication of a deeply buried conductor. This example illustrates how ignoring even small inclinations at the source dipole (one degree in this case) can give misleading results. This is particularly true in regions of high resistivity, such as the McCoy geothermal prospect, Nevada, where the secondary magnetic fields are sensitive to small tilts of the source dipole.

REFERENCES FOR APPENDIX A

Anderson, W.L., 1979, Numerical investigation of related Hankel transforms of orders 0 and 1 by adaptive digital filtering: Geophysics, v. 44, no. 7, p. 1287-1305.

Haught, J.R., Wilt, M.J., and Goldstein, N.E., 1981, Deep induction sounding for geothermal exploration from an arbitrarily oriented magnetic dipole (abstr.): Geophysics, v. 46, no. 4, p. 458.

Inman, J.R., 1975, Resistivity inversion with ridge regression: Geophysics, v. 40, no. 4, p. 798-817.

Lee, K.H., 1978, Electromagnetic scattering by a two-dimensional inhomogeneity due to an oscillating magnetic dipole (Ph.D. dissertation): Department of Engineering Geosciences, University of California, Berkeley. Lawrence Berkeley Laboratory, LBL-8275.

Morrison, H.F., Goldstein, N.E., Hoversten, M., Oppliger, G., and Riveros, C., 1978, Description, field test and data analysis of controlled source EM system (EM-60): Lawrence Berkeley Laboratory, LBL-7088.

Ryu, J., Morrison, H.F., and Ward, S.H., 1970, Electromagnetic fields about a loop source of current: Geophysics, v. 35, no. 5, p. 862-896.

Wilt, M., and Stark, M., 1982, A simple method for calculating apparent resistivity from electromagnetic sounding data: Geophysics, v. 47, no. 7, p. 1101-1105.

APPENDIX B

OBSERVED EM SOUNDING DATA AND CALCULATED LAYERED RESISTIVITY MODELS FOR DIXIE VALLEY

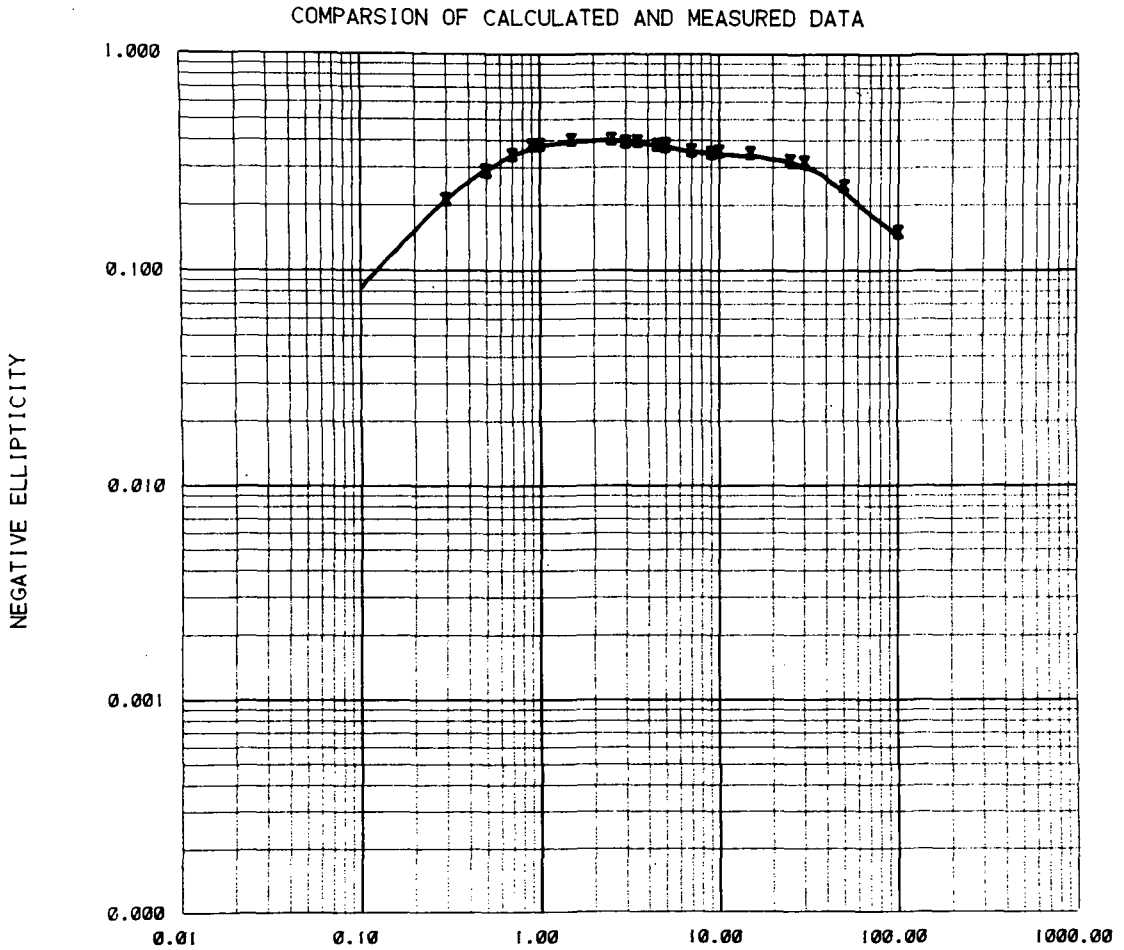

DV 10

CALCULATED DATA		MEASURED DATA		LAYER	RESISTIVITY(OHM-M)		THICKNESS(M)	
ELLIPTICITY	———	ELLIPTICITY	X	1	8.018	± .5517E-02	318.4	± 22.
				2	2.312	± .2736	455.8	± 142.
				3	659.6	± .5408E-05	.1000E+11	± 0.

DATA VARIENCE ESTIMATE .2420

XBL 829-11344

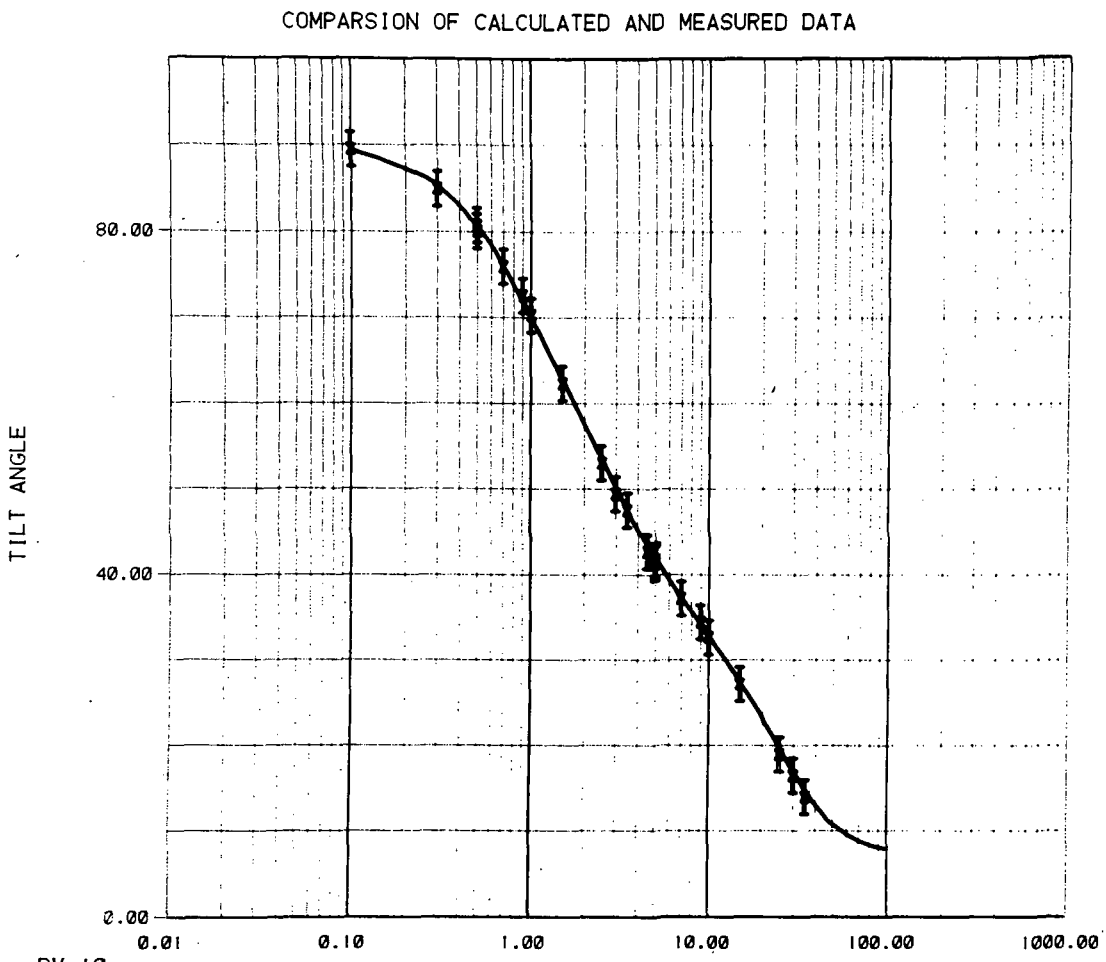

DV 10

CALCULATED DATA		MEASURED DATA		LAYER	RESISTIVITY(OHM-M)		THICKNESS(M)	
TILT ANGLE	———	TILT ANGLE	X	1	8.018	± .5517E-02	318.4	± 22.
				2	2.312	± .2736	455.8	± 142.
				3	659.6	± .5408E+05	.1000E+11	± 0.

DATA VARIENCE ESTIMATE .2420

XBL 829-11343

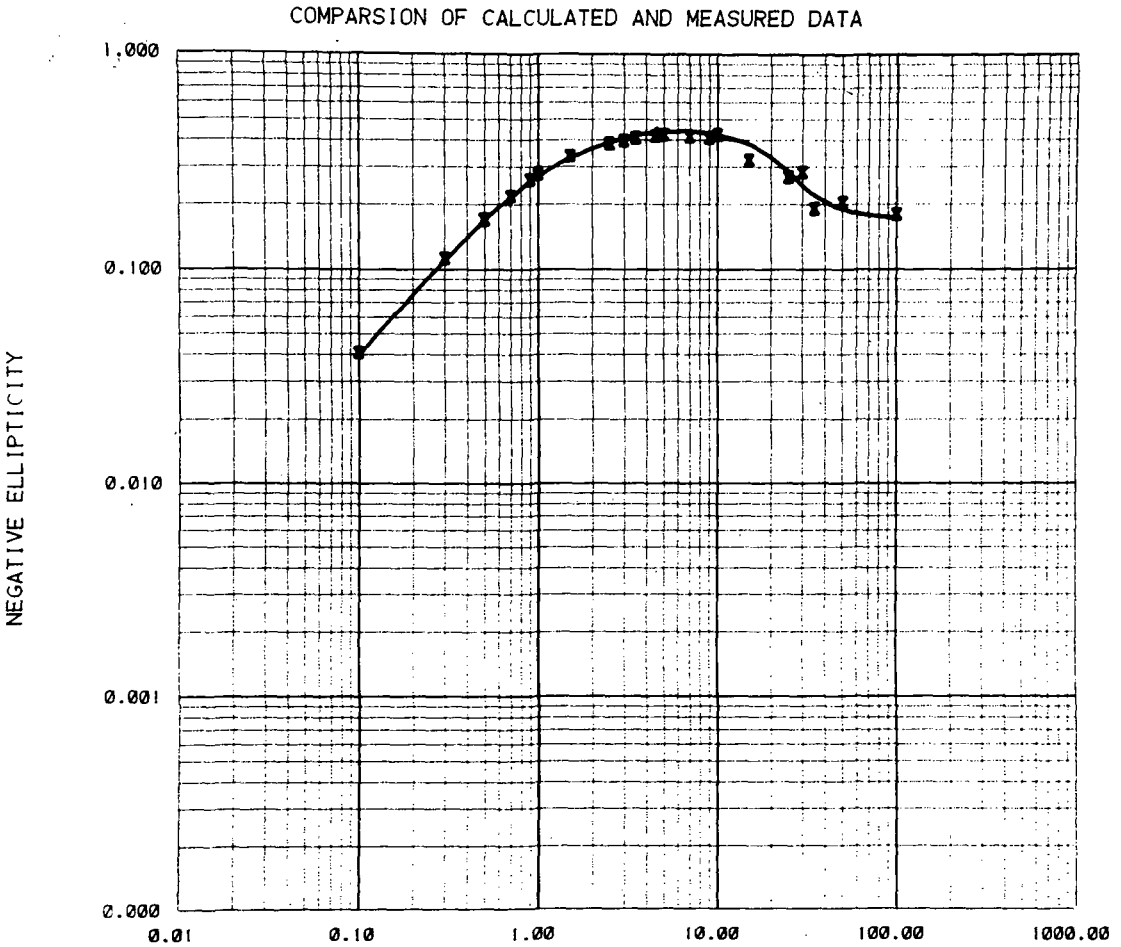

DV 11

CALCULATED DATA — ELLIPTICITY

MEASURED DATA — ELLIPTICITY

	LAYER	RESISTIVITY(OHM-M)		THICKNESS(M)	
X	1	26.73	± .3878E-02	144.0	± 15.
	2	5.151	± .6215	231.1	± 71.
	3	13.53	± 2.462	.1000E+11	± 0.

DATA VARIENCE ESTIMATE 2.505

XBL 829-11346

COMPARSION OF CALCULATED AND MEASURED DATA

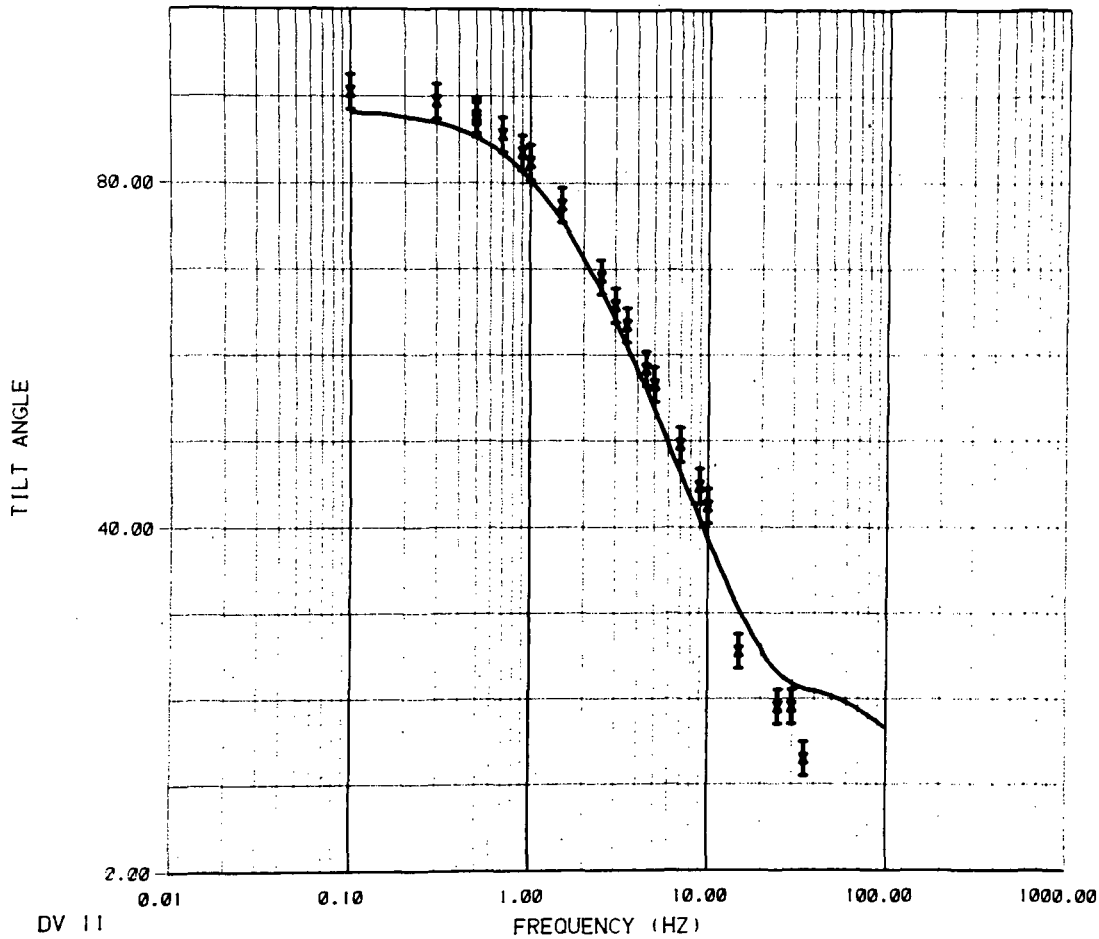

DV 11

CALCULATED DATA
TILT ANGLE ——— MEASURED DATA
TILT ANGLE

	LAYER	RESISTIVITY(OHM-M)		THICKNESS(M)	
X	1	26.73	± .3878E-02	144.0	± 15.
	2	5.151	± .6215	231.1	± 71.
	3	13.53	± 2.462	.1000E+11	± 0.

DATA VARIENCE ESTIMATE 2.505

XBL 829-11345

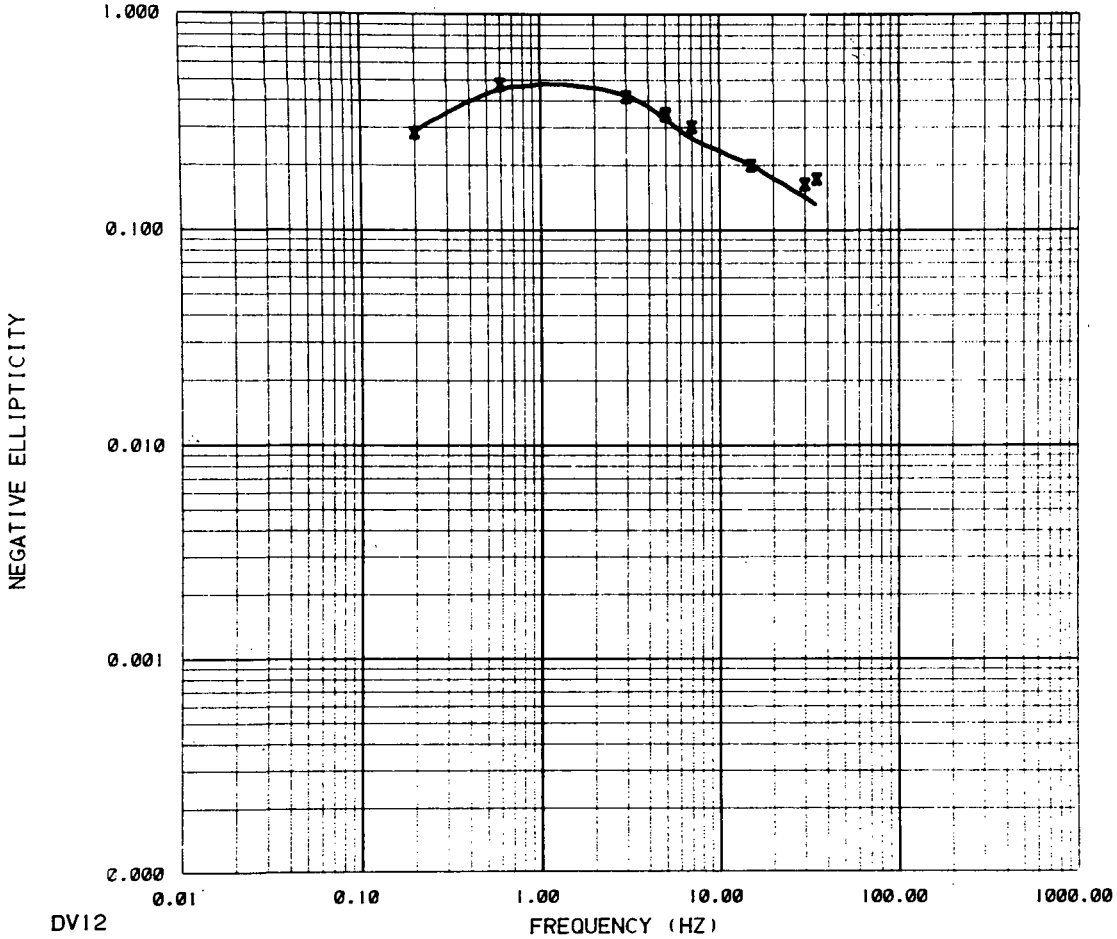

DV12

CALCULATED DATA — ELLIPTICITY

MEASURED DATA — ELLIPTICITY

	LAYER	RESISTIVITY(OHM-M)		THICKNESS(M)	
X	1	9.069	± .9373E-02	386.0	± 69.
	2	4.756	± .6254	704.0	± 201.
	3	911.5	± .4198E+05	.1000E+11	± 0.

DATA VARIENCE ESTIMATE 4.204

XBL 829-11358

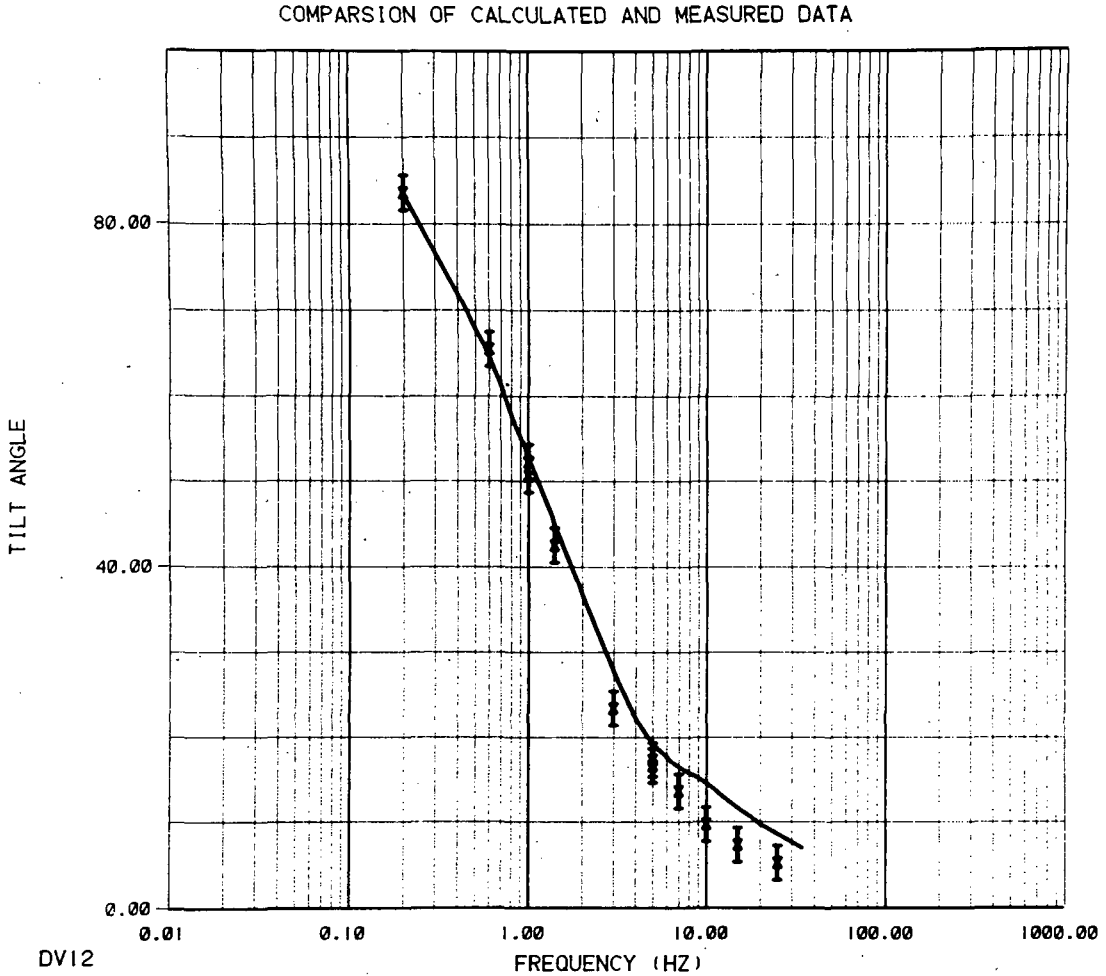

DV12

CALCULATED DATA		MEASURED DATA		LAYER	RESISTIVITY(OHM-M)		THICKNESS(M)	
TILT ANGLE	———	TILT ANGLE	X	1	9.069	± .9373E-02	386.0	± 69.
				2	4.756	± .6254	704.0	± 201.
				3	911.5	± .4198E+05	.1000E+11	± 0.

DATA VARIENCE ESTIMATE 4.204

XBL 829-11357

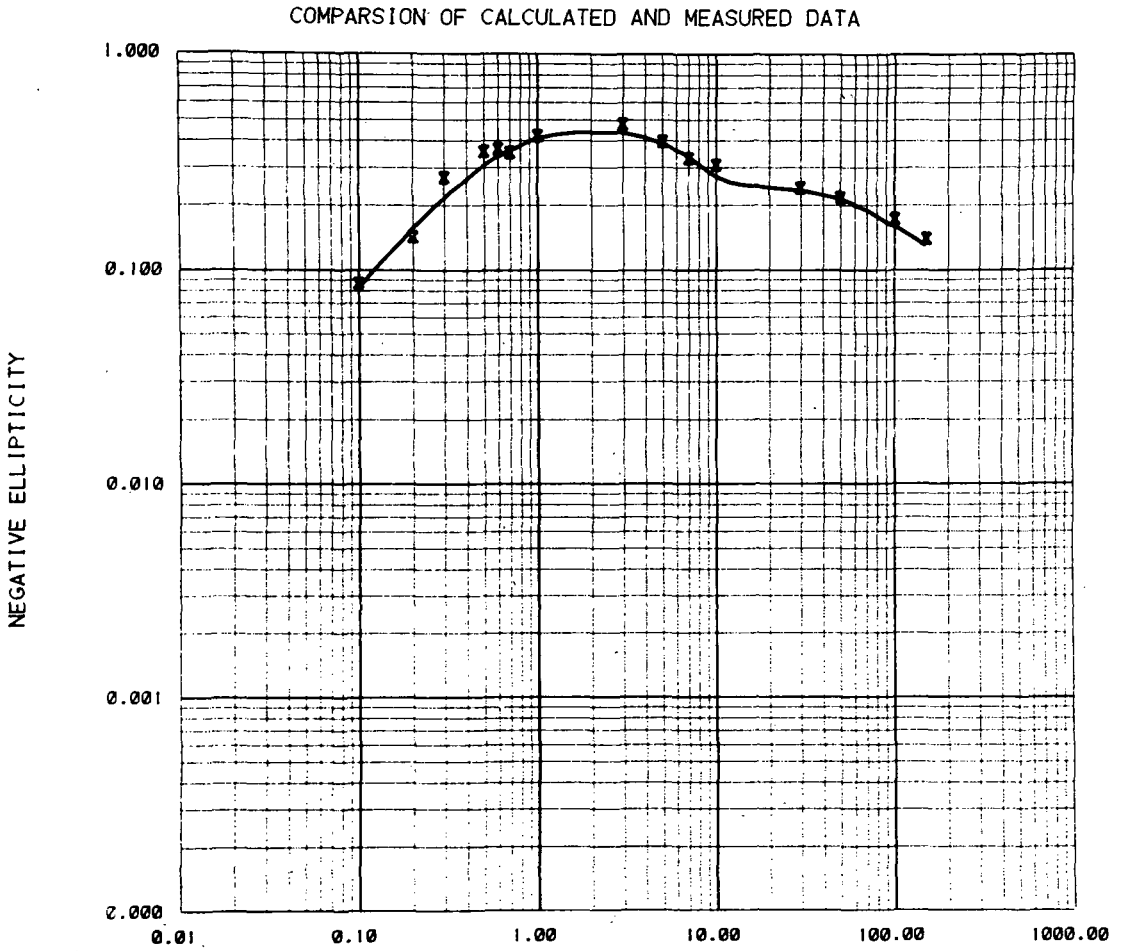

DV 14

CALCULATED DATA — ELLIPTICITY

MEASURED DATA — ELLIPTICITY

	LAYER	RESISTIVITY(OHM-M)		THICKNESS(M)	
X	1	27.05	± .5990E-02	379.6	± 27.
	2	5.193	± .9629	453.1	± 149.
	3	124.6	± 283.5	.1000E+11	± 0.

DATA VARIENCE ESTIMATE 2.316

XBL 829-11348

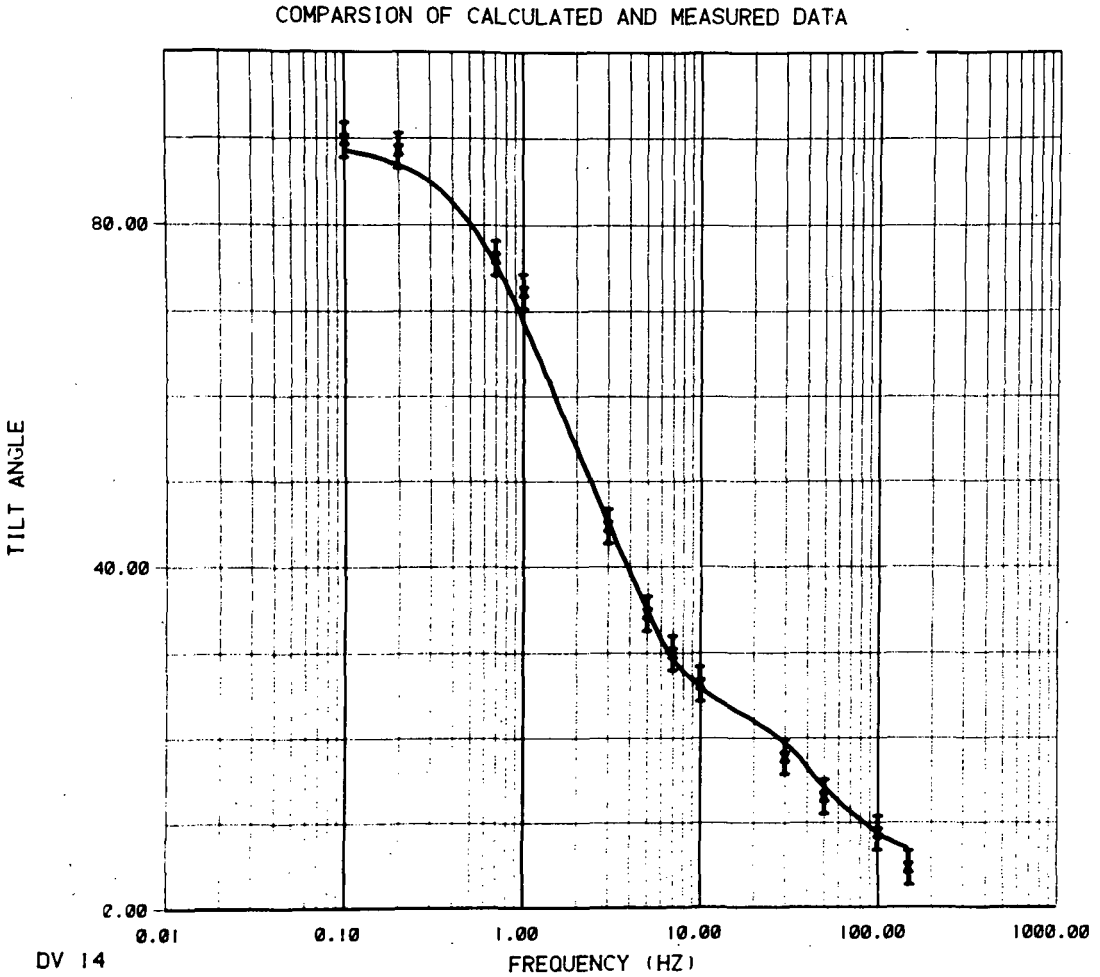

DV 14

CALCULATED DATA — MEASURED DATA

TILT ANGLE ——— TILT ANGLE

	LAYER	RESISTIVITY(OHM-M)		THICKNESS(M)	
X	1	27.05	± .5990E-02	379.6	± 27.
	2	5.193	± .9629	453.1	± 149.
	3	124.6	± 283.5	.1000E+11	± 0.

DATA VARIENCE ESTIMATE 2.316

XBL 829-11347

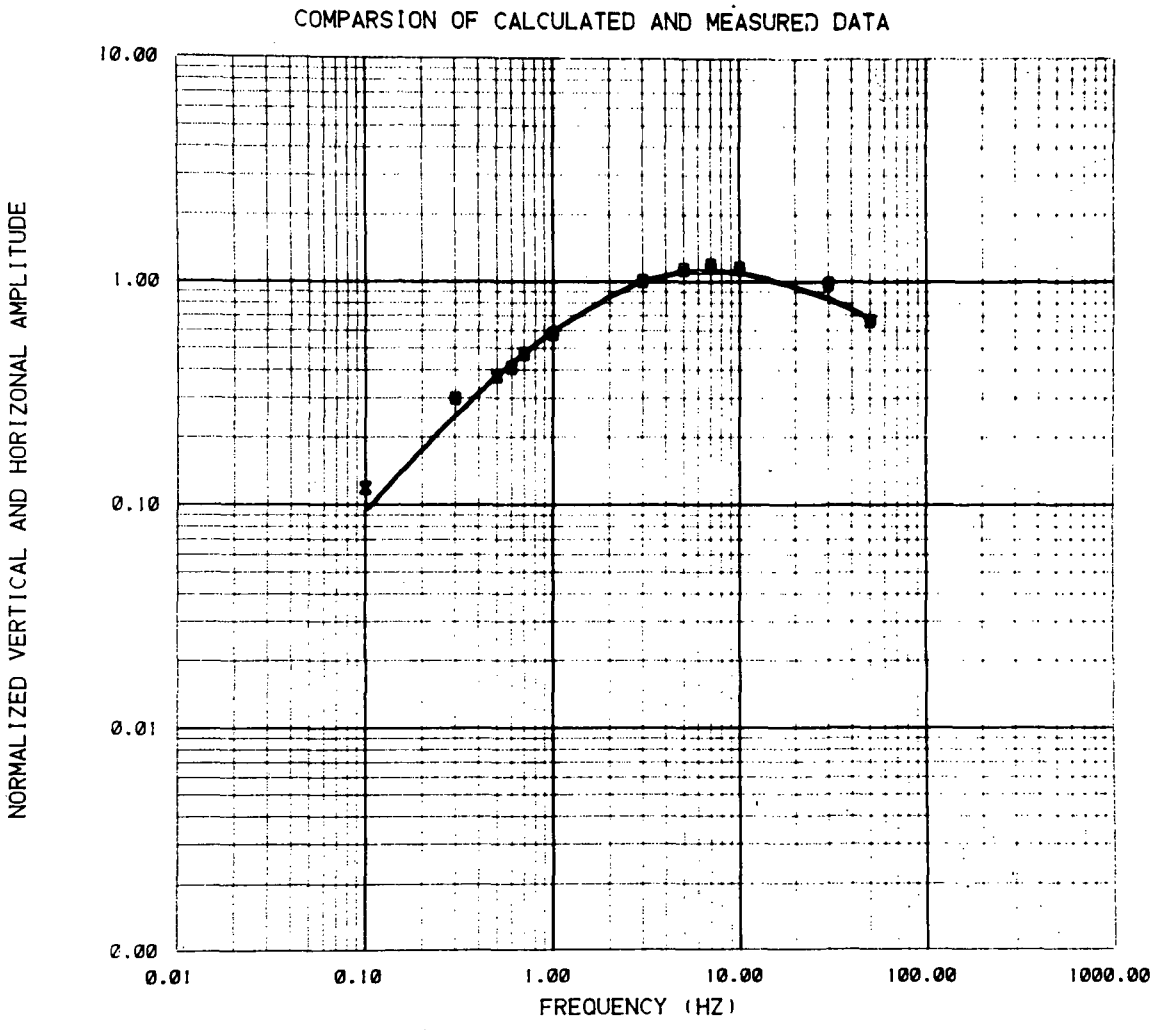

DV 15

		LAYER	RESISTIVITY (OHM-M)	THICKNESS (M)
CALCULATED ——				
MEASURED	x	1	6.34 ± .19	205.3 ± 10
		2	2.16 ± .05	∞

DATA VARIENCE ESTIMATE .242

XBL 829-11653

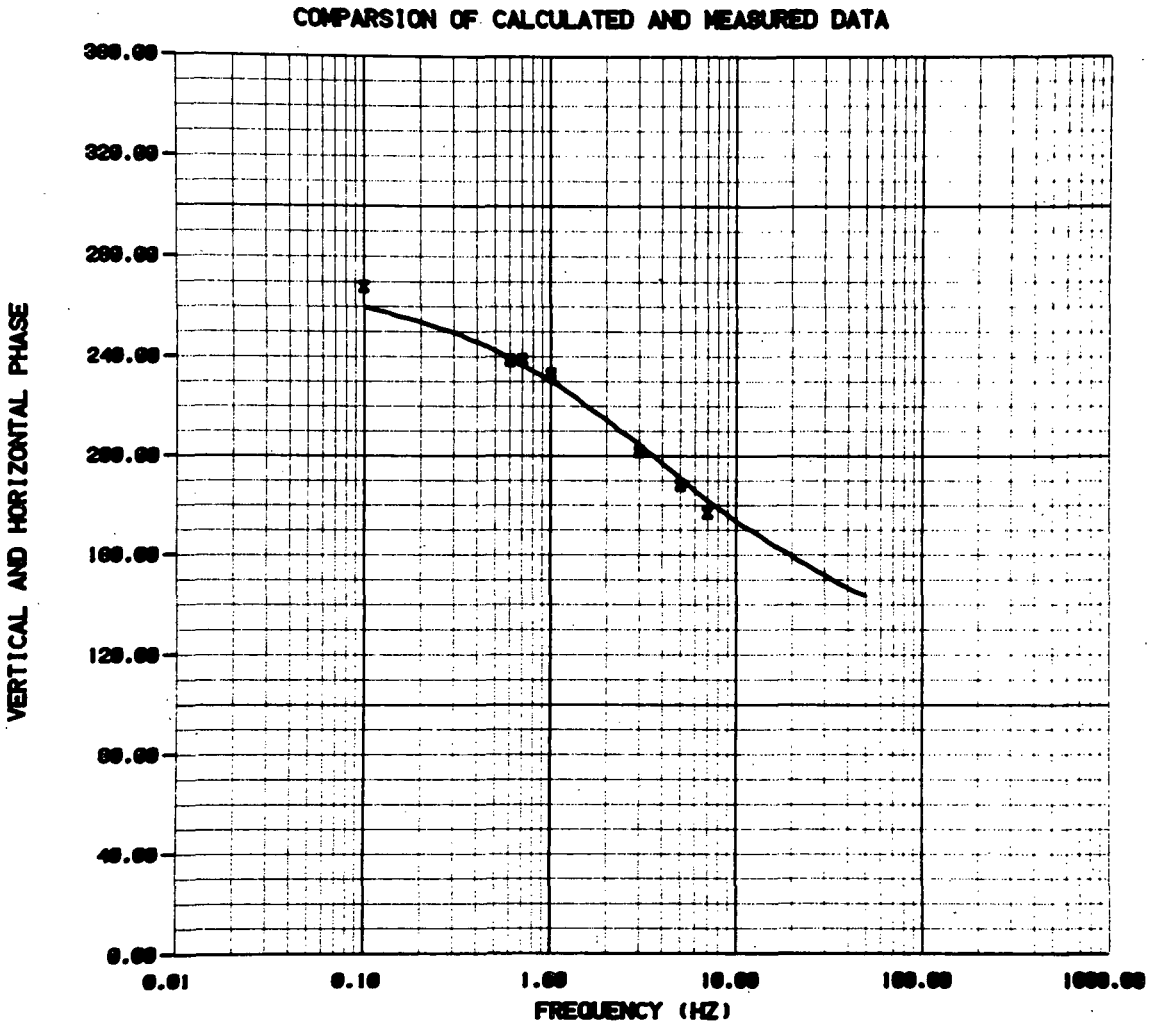

DV 15

CALCULATED ——		LAYER	RESISTIVITY (OHM-M)	THICKNESS (M)
MEASURED	x	1	6.34 ± .19	205.3 ± 10
		2	2.16 ± .05	∞

DATA VARIENCE ESTIMATE .242

XBL 829-11649

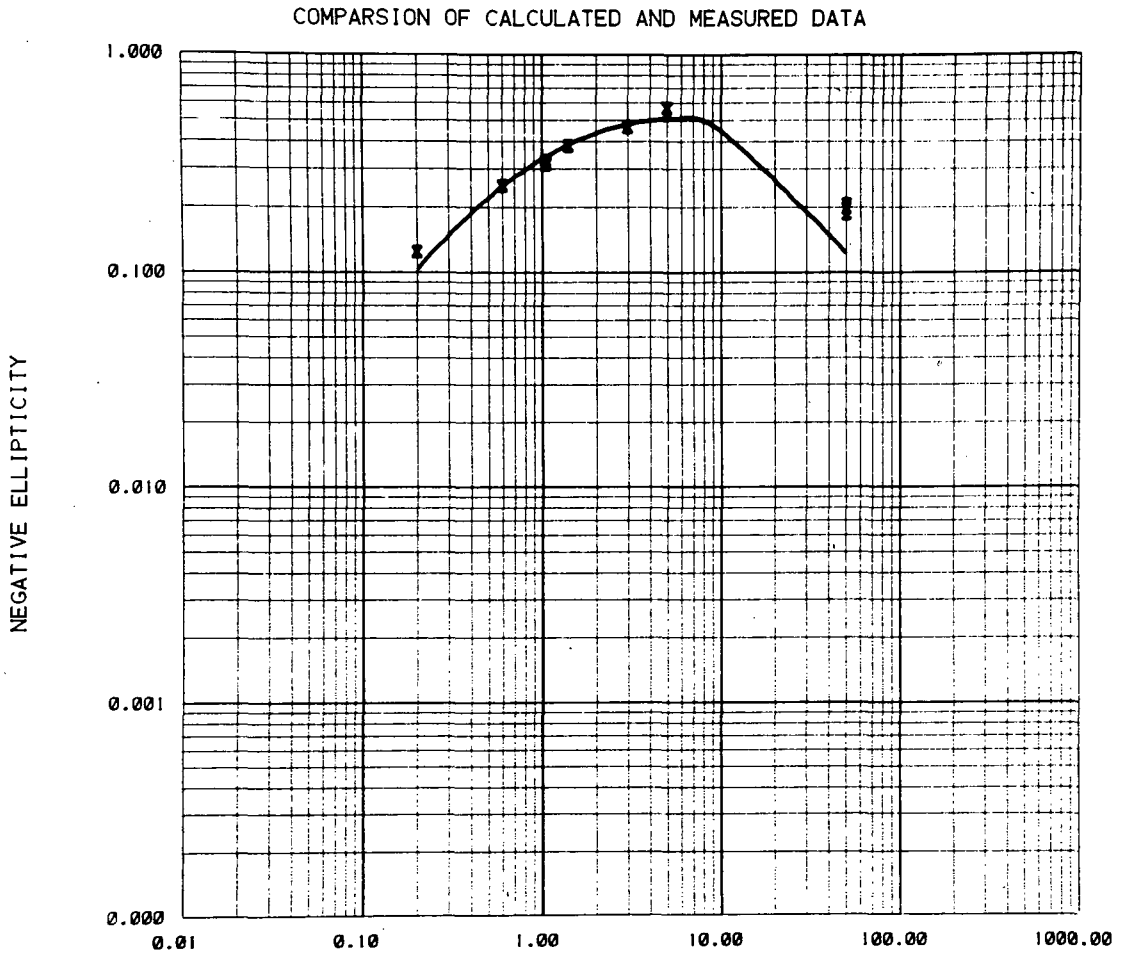

DV 16

CALCULATED DATA		MEASURED DATA		LAYER	RESISTIVITY(OHM-M)		THICKNESS(M)	
ELLIPTICITY	———	ELLIPTICITY	X	1	30.46	± .5735E-02	573.2	± 72.
				2	74.93	± 13.28	.1000E+11	± 0.

DATA VARIENCE ESTIMATE 2.909

XBL 829-11349

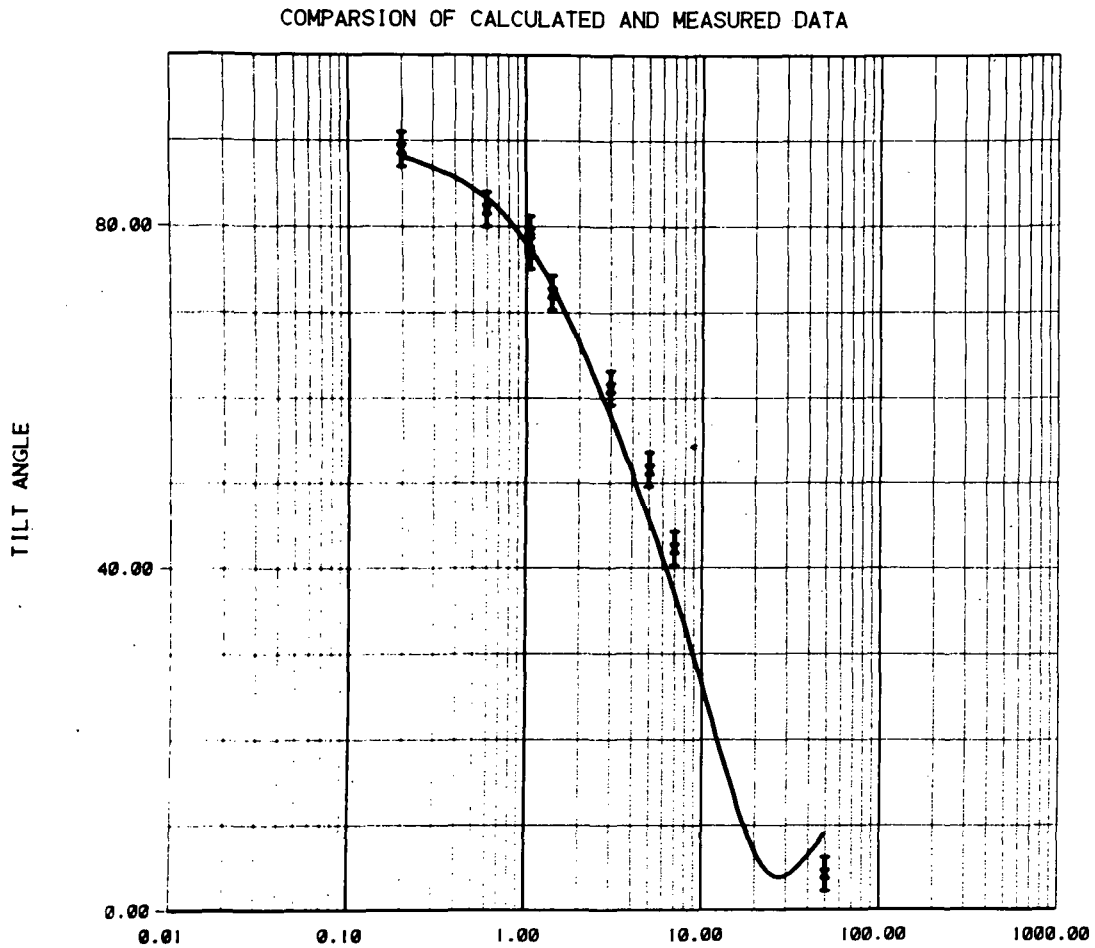
COMPARSION OF CALCULATED AND MEASURED DATA
80.00
40.00
0.00
TILT ANGLE
0.01
0.10
1.00
10.00
100.00
1000.00
FREQUENCY (HZ)
DV 16
CALCULATED DATA
TILT ANGLE
MEASURED DATA
TILT ANGLE
LAYER RESISTIVITY(OHM-M) THICKNESS(M)
X 1 30.46 ± .5735E-02 573.2 ± 72.
2 74.93 ± 13.28 .1000E+11 ± 0.
DATA VARIENCE ESTIMATE 2.909
XBL 829-11350

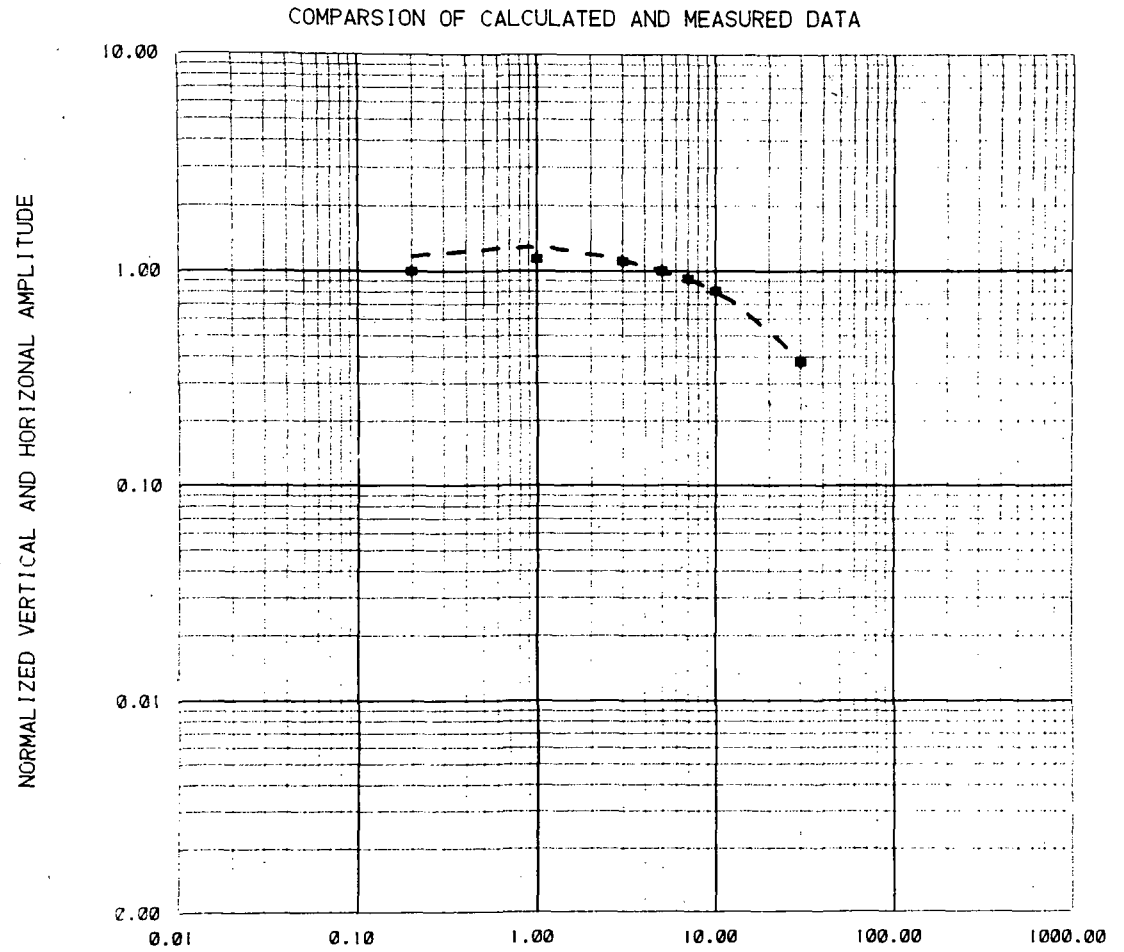

DV 17

CALCULATED DATA		MEASURED DATA		LAYER	RESISTIVITY(OHM-M)		THICKNESS(M)	
HR	———————	HR	X	1	8.984	± .2634E-02	408.6	± 2.
HZ	— — —	HZ	*	2	1.561	± .3035E-01	.1000E+11	± 0.

DATA VARIENCE ESTIMATE 82.75

XBL 829-11339

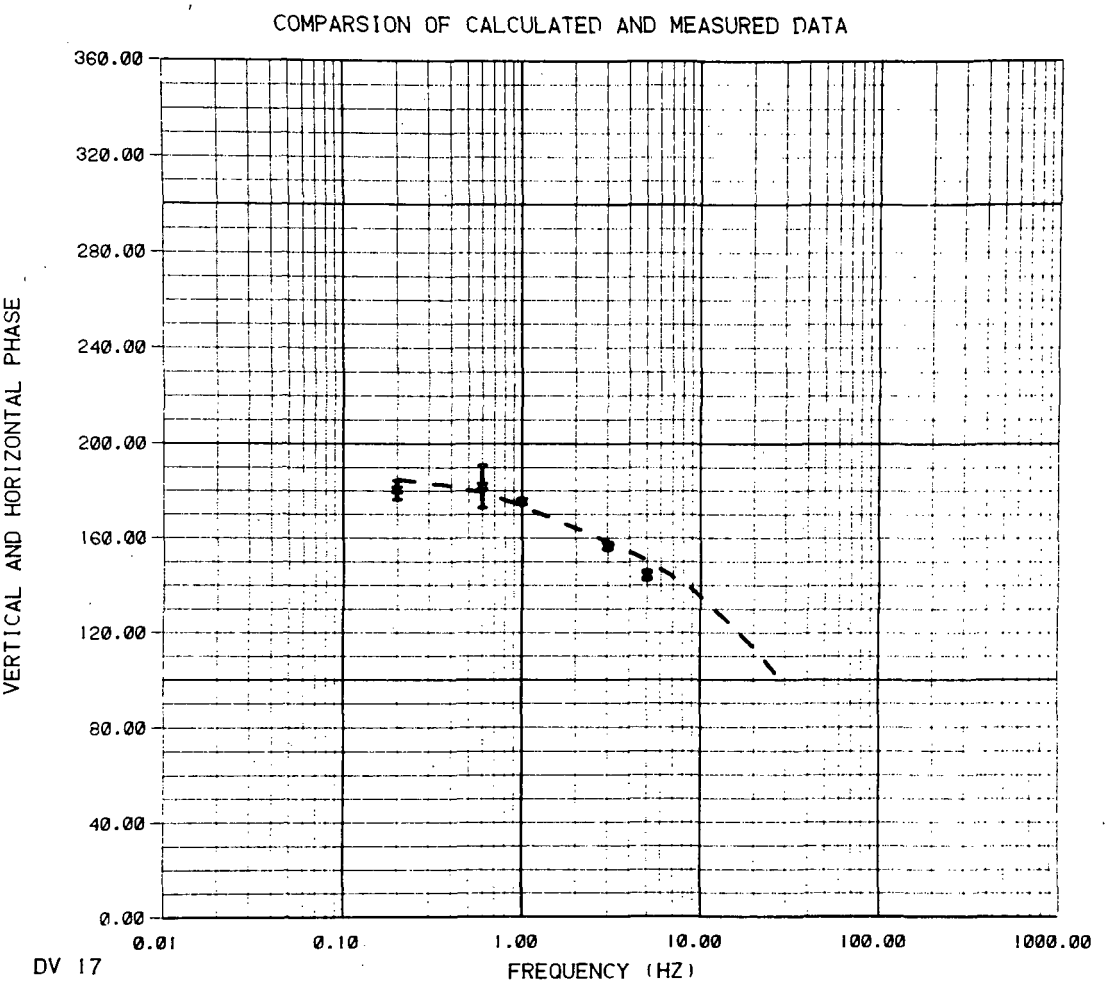

DV 17

CALCULATED DATA		MEASURED DATA		LAYER	RESISTIVITY(OHM-M)		THICKNESS(M)		
HR	———————	HR	X	1	8.984	± .2634E-02	408.6	±	2.
HZ	— — —	HZ	*	2	1.561	± .3035E-01	.1000E+11	±	0.

DATA VARIENCE ESTIMATE 82.75

XBL 829-11340

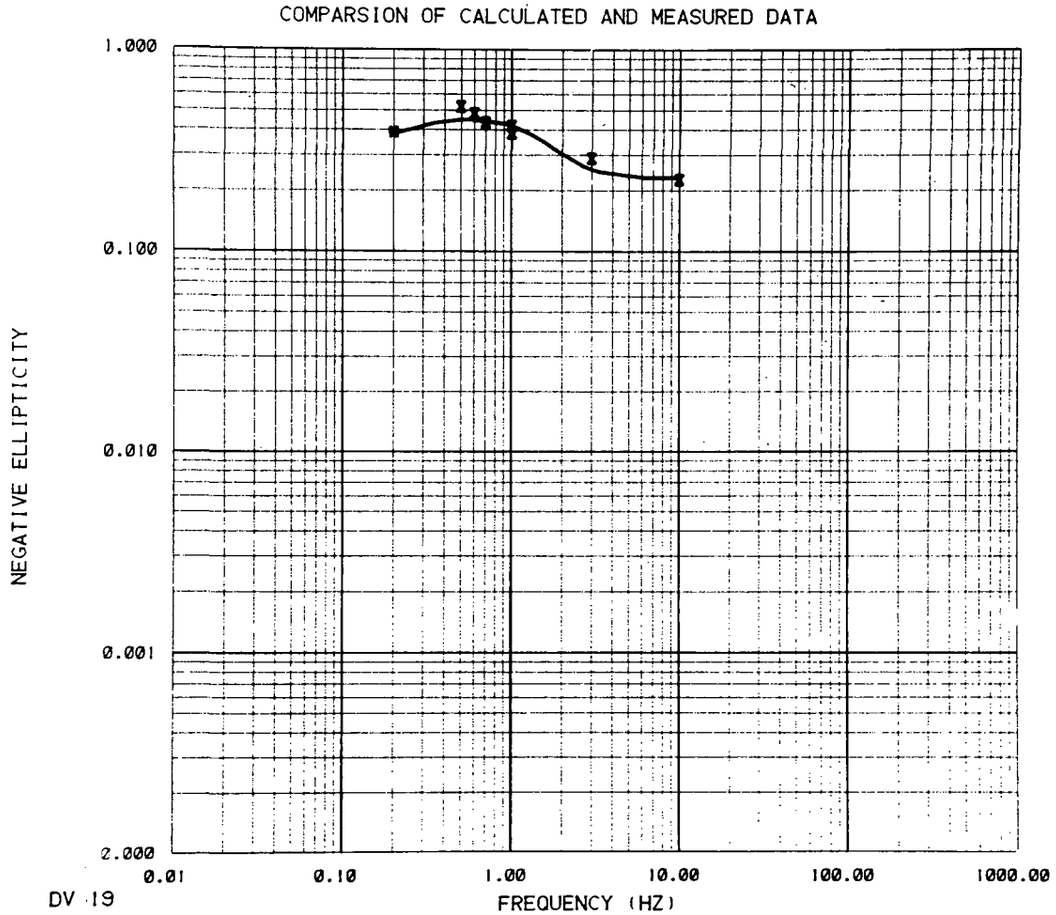

DV 19

CALCULATED DATA — ELLIPTICITY

MEASURED DATA — ELLIPTICITY

	LAYER	RESISTIVITY(OHM-M)		THICKNESS(M)	
X	1	13.46	± .1153E-01	552.5	± 51.
	2	2.597	± .5193	639.3	± 195.
	3	7440.	± .3356E+07	.1000E+11	± 0.

DATA VARIENCE ESTIMATE 4.972

XBL 829-11355

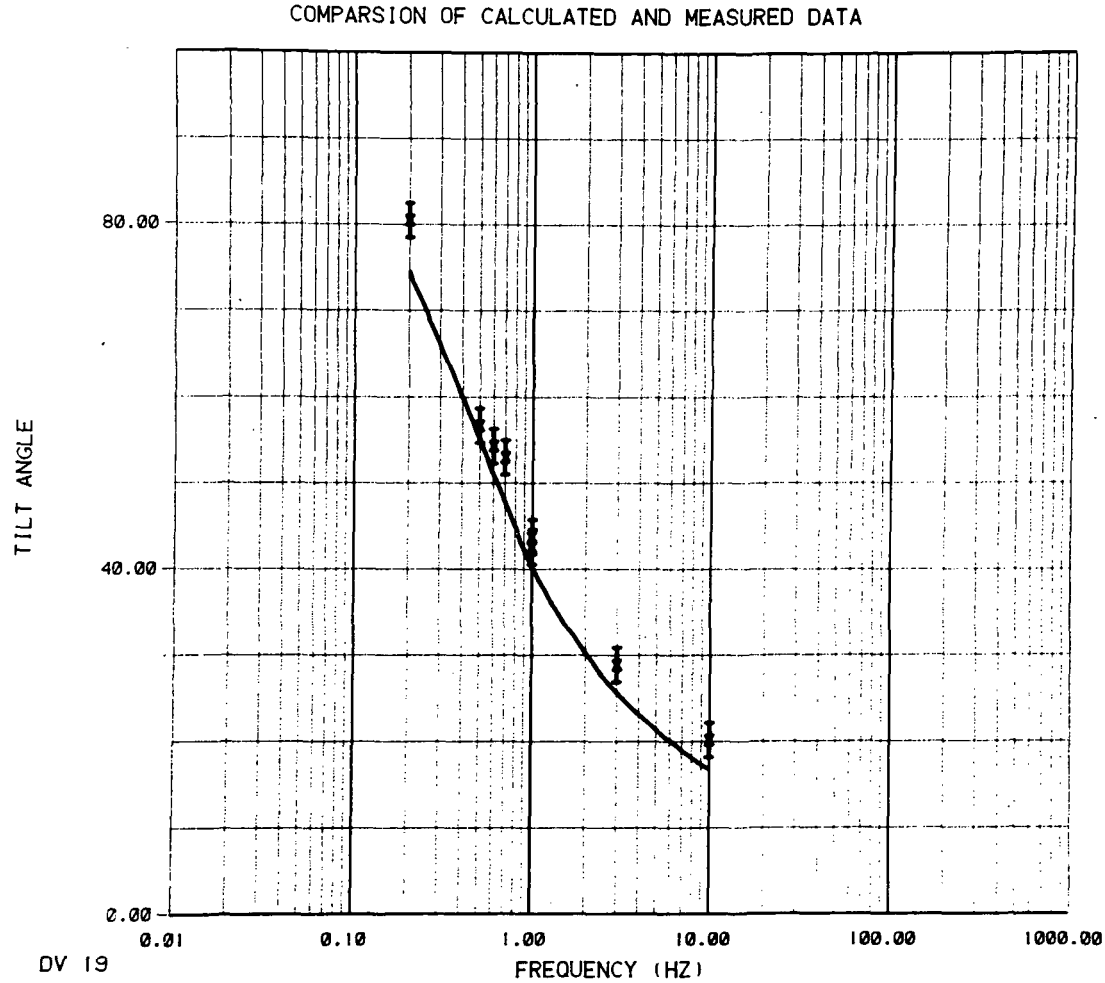

DV 19

CALCULATED DATA		MEASURED DATA		LAYER	RESISTIVITY(OHM-M)		THICKNESS(M)	
TILT ANGLE	———	TILT ANGLE	X	1	13.46	± .1153E-01	552.5	± 51.
				2	2.597	± .5193	639.3	± 195.
				3	7440.	± .3356E+07	.1000E+11	± 0.

DATA VARIENCE ESTIMATE 4.972

XBL 829-11356

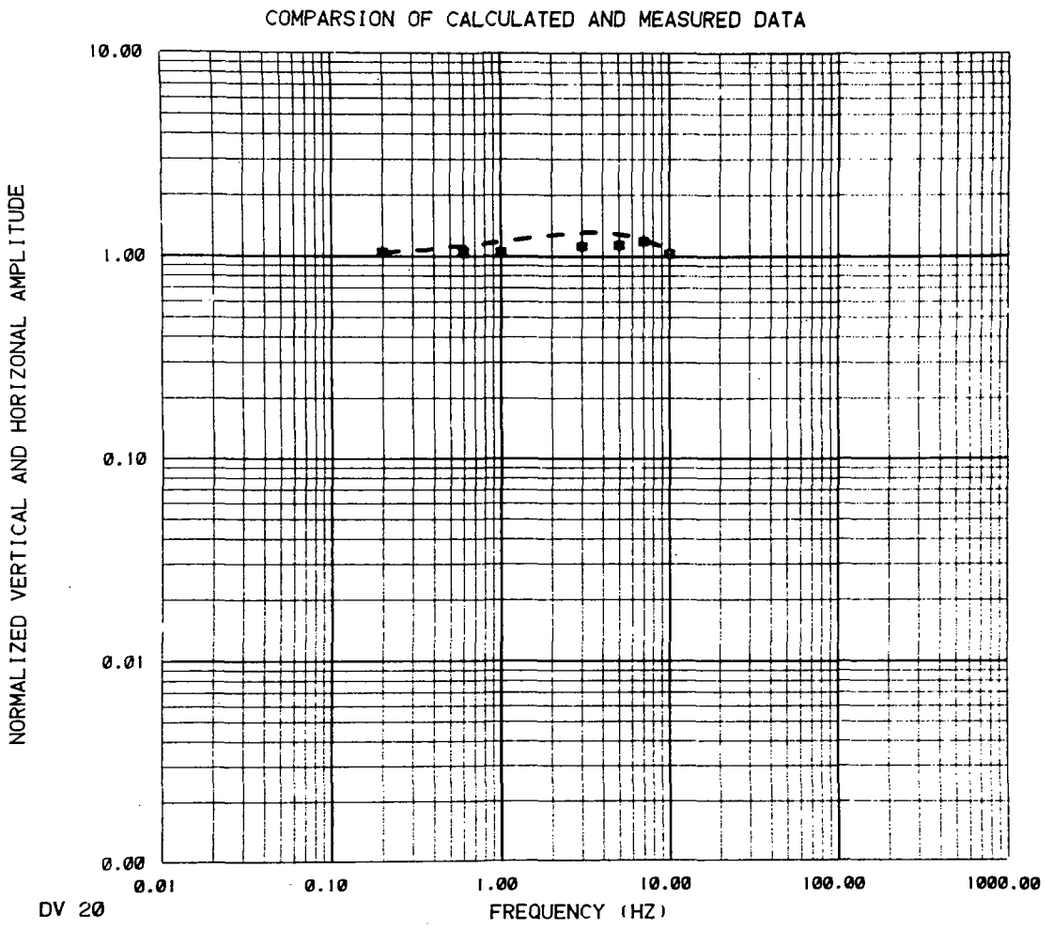

DV 20

CALCULATED DATA		MEASURED DATA		LAYER	RESISTIVITY(OHM-M)		THICKNESS(M)	
HR	———————	HR	X	1	.8342E+05±	.2905E-02	56.99 ±	12.
HZ	— — —	HZ	*	2	4.342 ±	.2067	.1000E+11±	0.

DATA VARIENCE ESTIMATE 24.05

XBL 829-11365

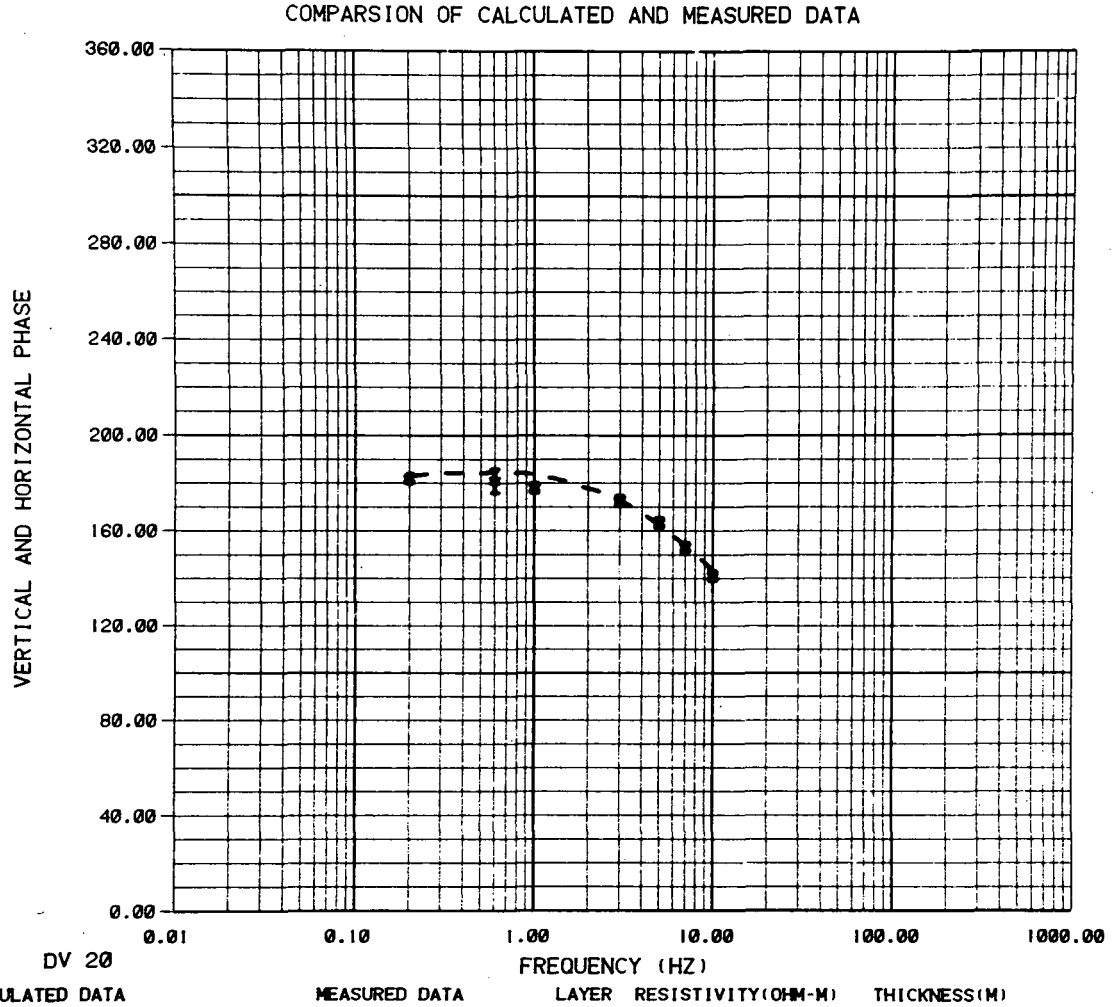

XBL 829-11364

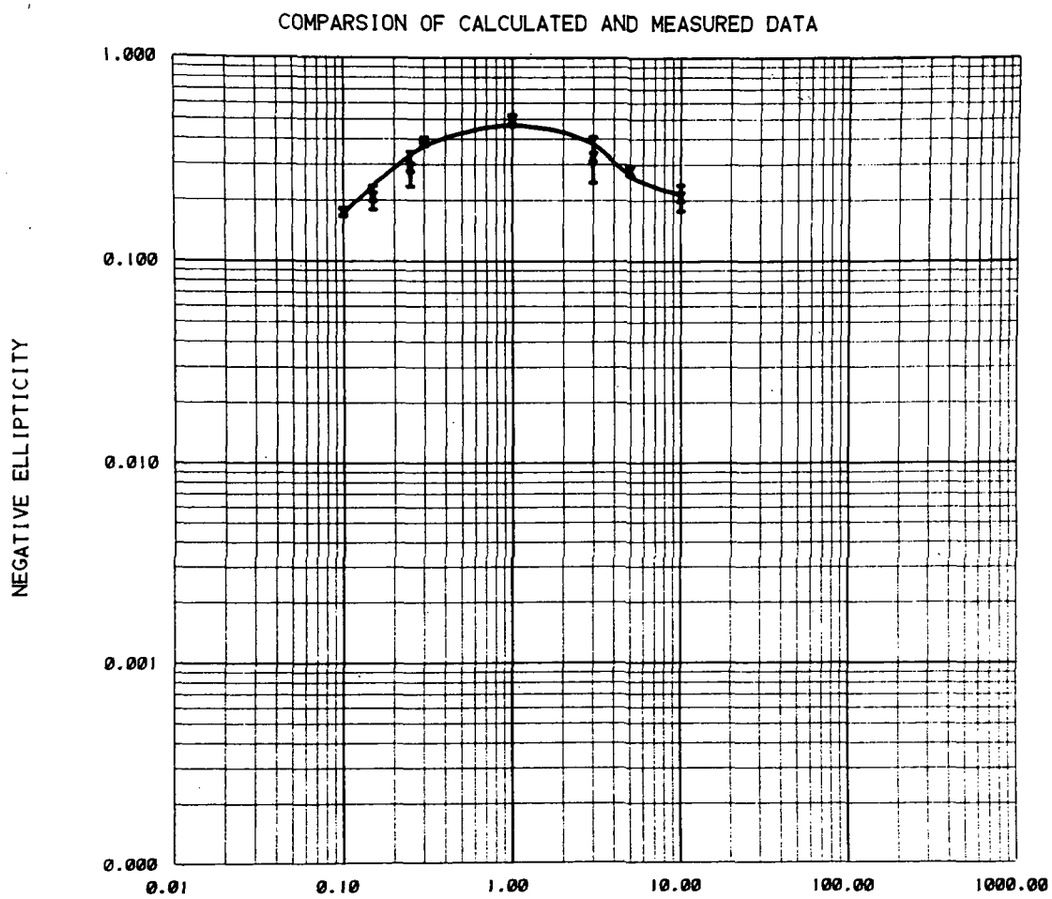

DV 21

CALCULATED DATA — ELLIPTICITY

MEASURED DATA — ELLIPTICITY

	LAYER	RESISTIVITY(OHM-M)		THICKNESS(M)	
X	1	22.40	± .8699E-02	524.5	± 48.
	2	5.747	± .8804	682.5	± 159.
	3	588.0	± 3569.	.1000E+11	± 0.

DATA VARIENCE ESTIMATE 8.736

XBL 829-11351

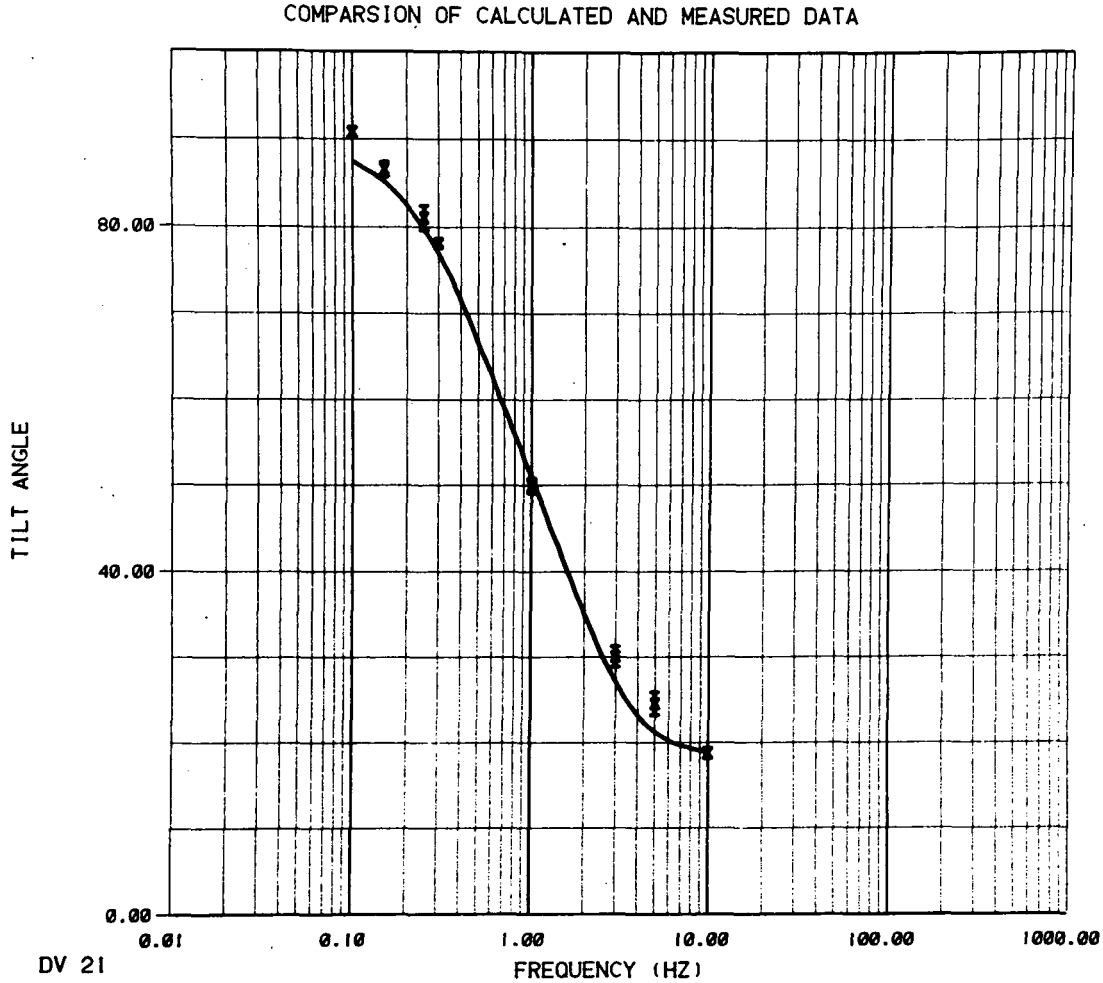

DV 21

CALCULATED DATA		MEASURED DATA		LAYER	RESISTIVITY(OHM-M)		THICKNESS(M)	
TILT ANGLE	———	TILT ANGLE	X	1	22.40	± .8699E-02	524.5	± 48.
				2	5.747	± .8804	682.5	± 159.
				3	588.0	± 3569.	.1000E+11	± 0.

DATA VARIENCE ESTIMATE 8.736

XBL 829-11352

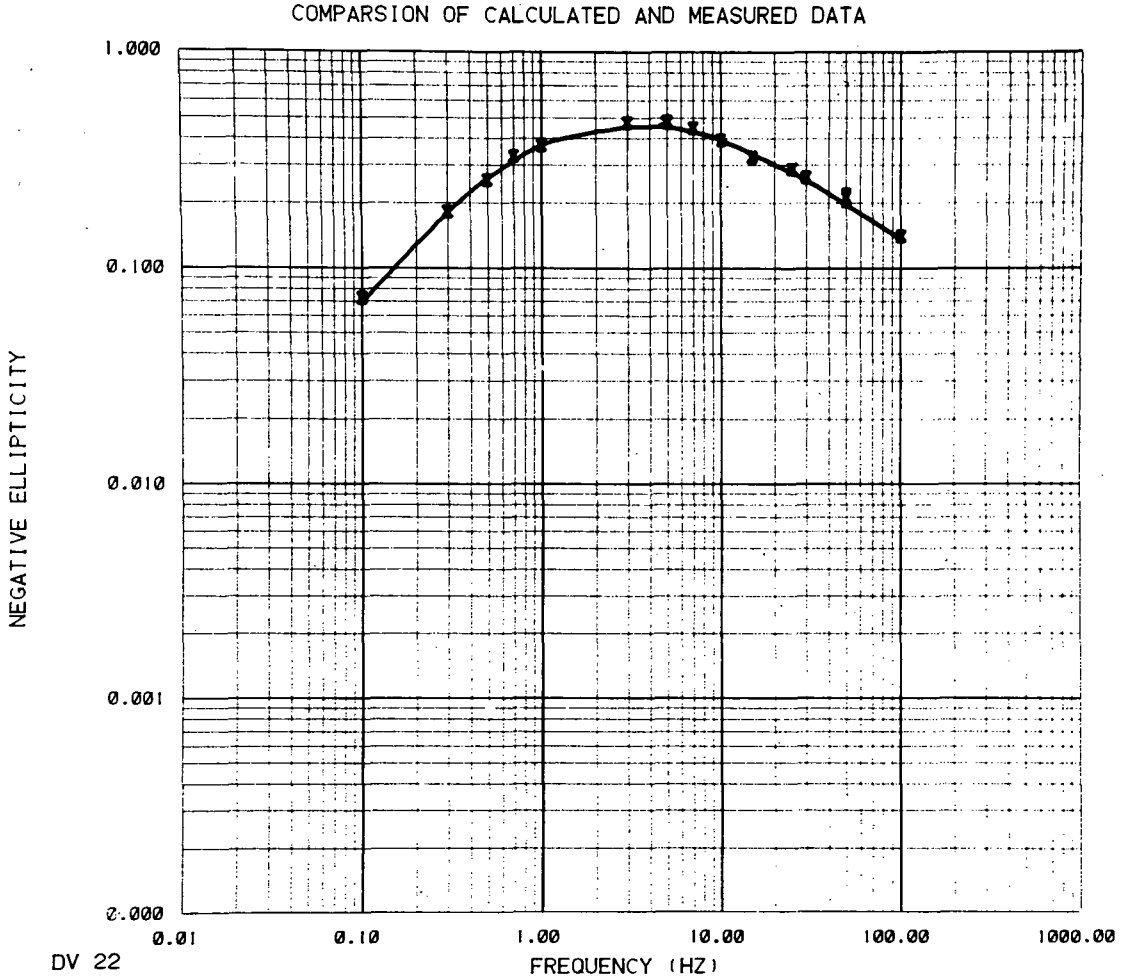

DV 22

CALCULATED DATA — ELLIPTICITY

MEASURED DATA — ELLIPTICITY

	LAYER	RESISTIVITY(OHM-M)		THICKNESS(M)	
X	1	6.848	± .5288E-02	231.9	± 43.
	2	3.566	± .7169	332.5	± 192.
	3	12.71	± 9.018	.1000E+11	± 0.

DATA VARIENCE ESTIMATE .5562

XBL 829-11360

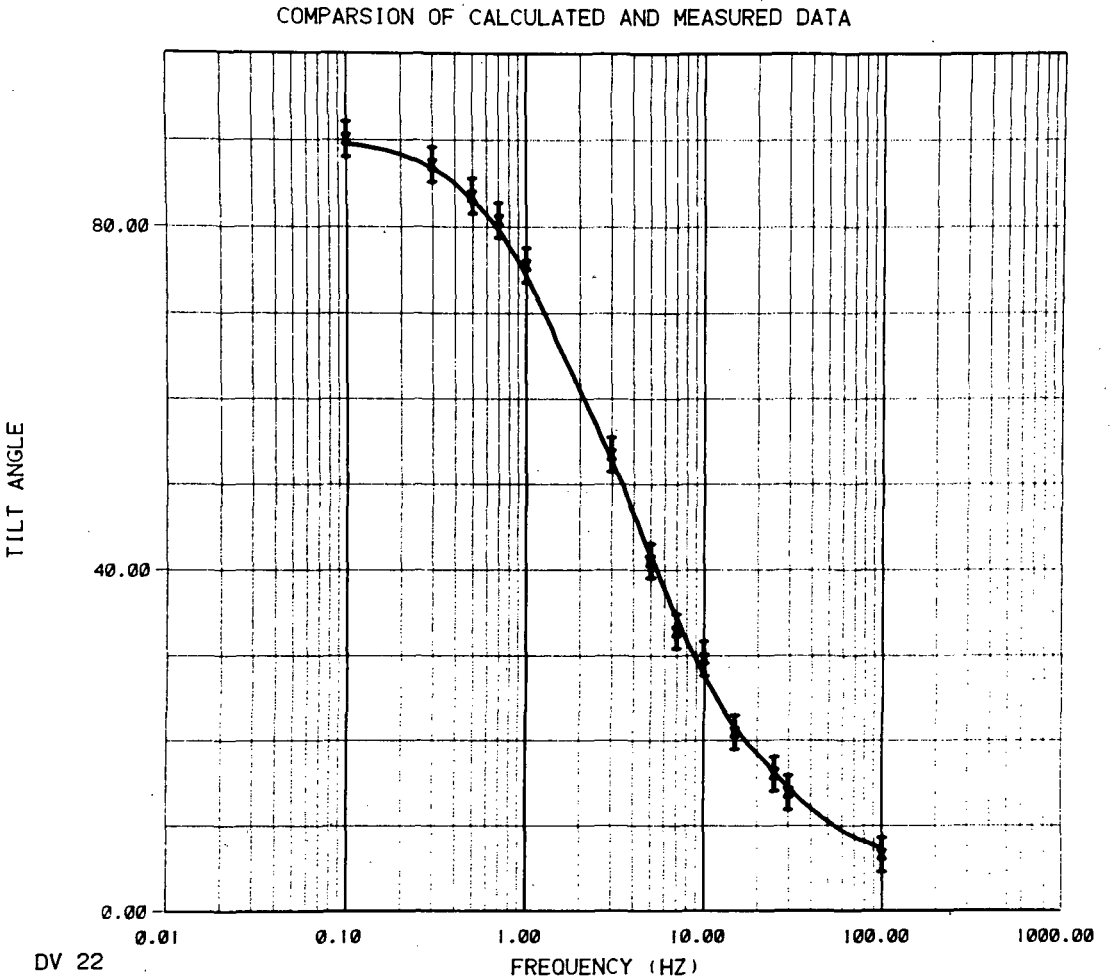

DV 22

CALCULATED DATA		MEASURED DATA		LAYER	RESISTIVITY(OHM-M)		THICKNESS(M)	
TILT ANGLE	———	TILT ANGLE	X	1	6.848	± .5288E-02	231.9	± 43.
				2	3.566	± .7169	332.5	± 192.
				3	12.71	± 9.018	.1000E+11	± 0.

DATA VARIENCE ESTIMATE .5562

XBL 829-11359

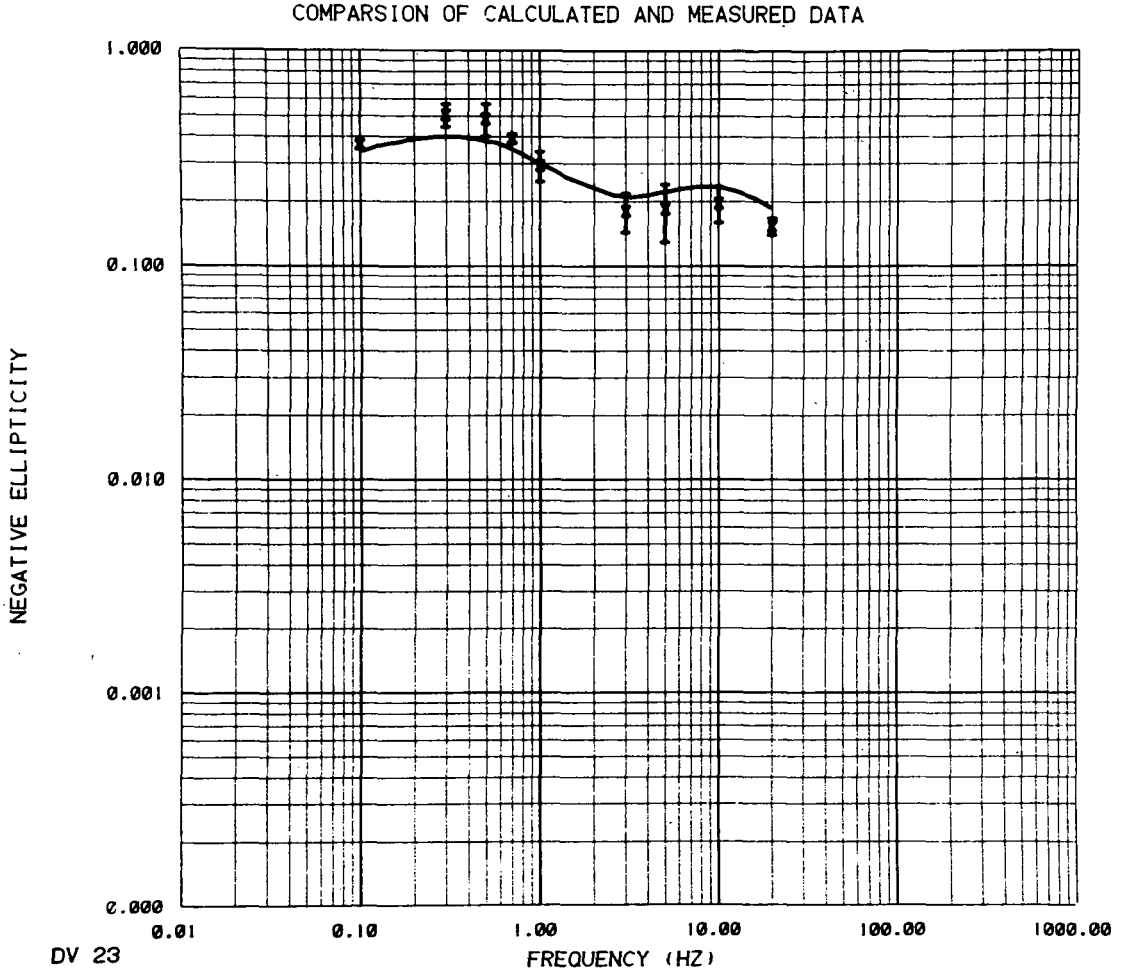

DV 23

CALCULATED DATA		MEASURED DATA		LAYER	RESISTIVITY(OHM-M)		THICKNESS(M)	
ELLIPTICITY	———	ELLIPTICITY	X	1	20.00	± .1875E-02	745.2	± 50.
				2	1.845	± .4845	450.5	± 215.
				3	6.074	± 1.488	.1000E+11	± 0.

DATA VARIENCE ESTIMATE 27.12

XBL 829-11354

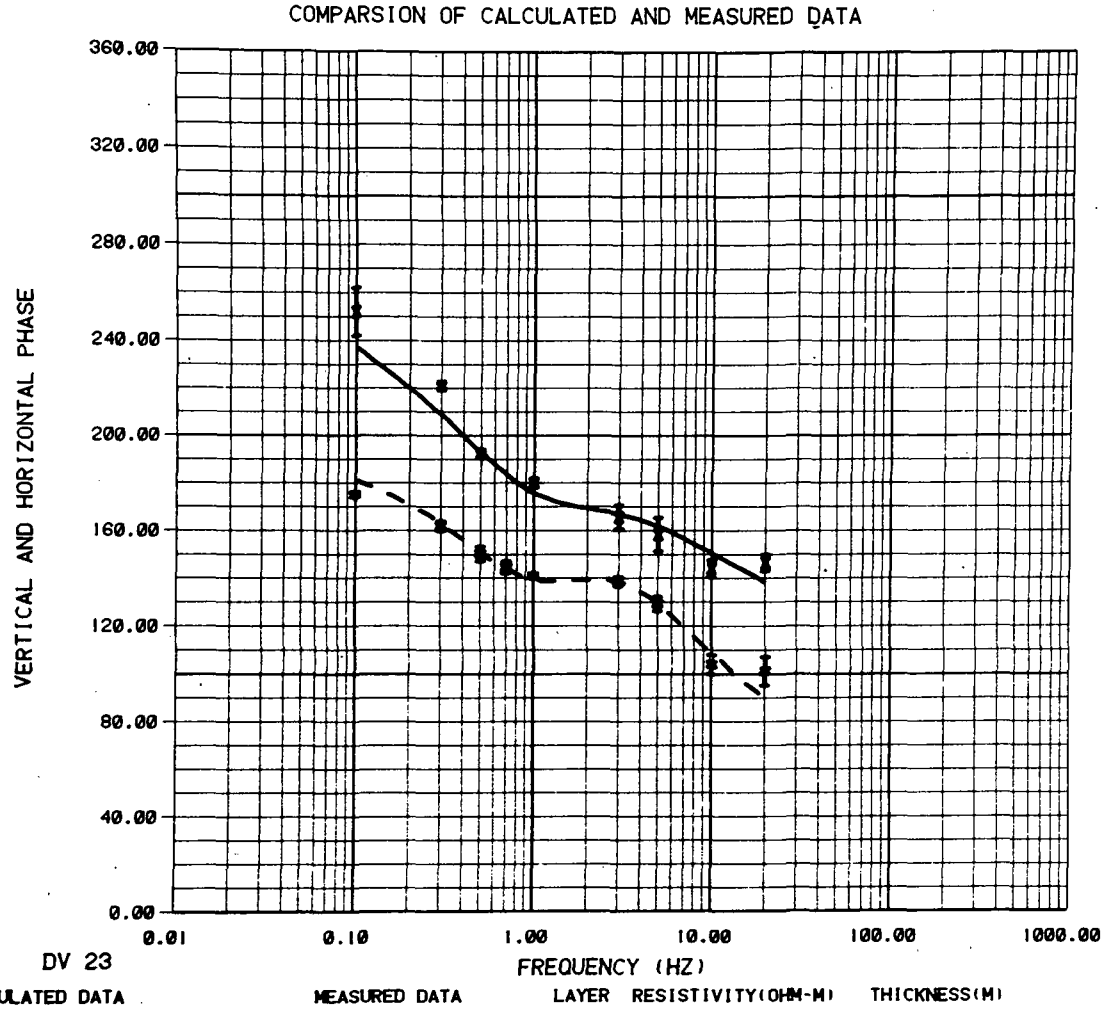

DV 23

CALCULATED DATA		MEASURED DATA		LAYER	RESISTIVITY(OHM-M)		THICKNESS(M)	
HR	———	HR	X	1	20.00	± .1875E-02	745.2	± 50.
HZ	— — —	HZ	*	2	1.845	± .4845	450.5	± 215.
				3	6.074	± 1.488	.1000E+11	± 0.

DATA VARIENCE ESTIMATE 27.12

XBL 829-11353

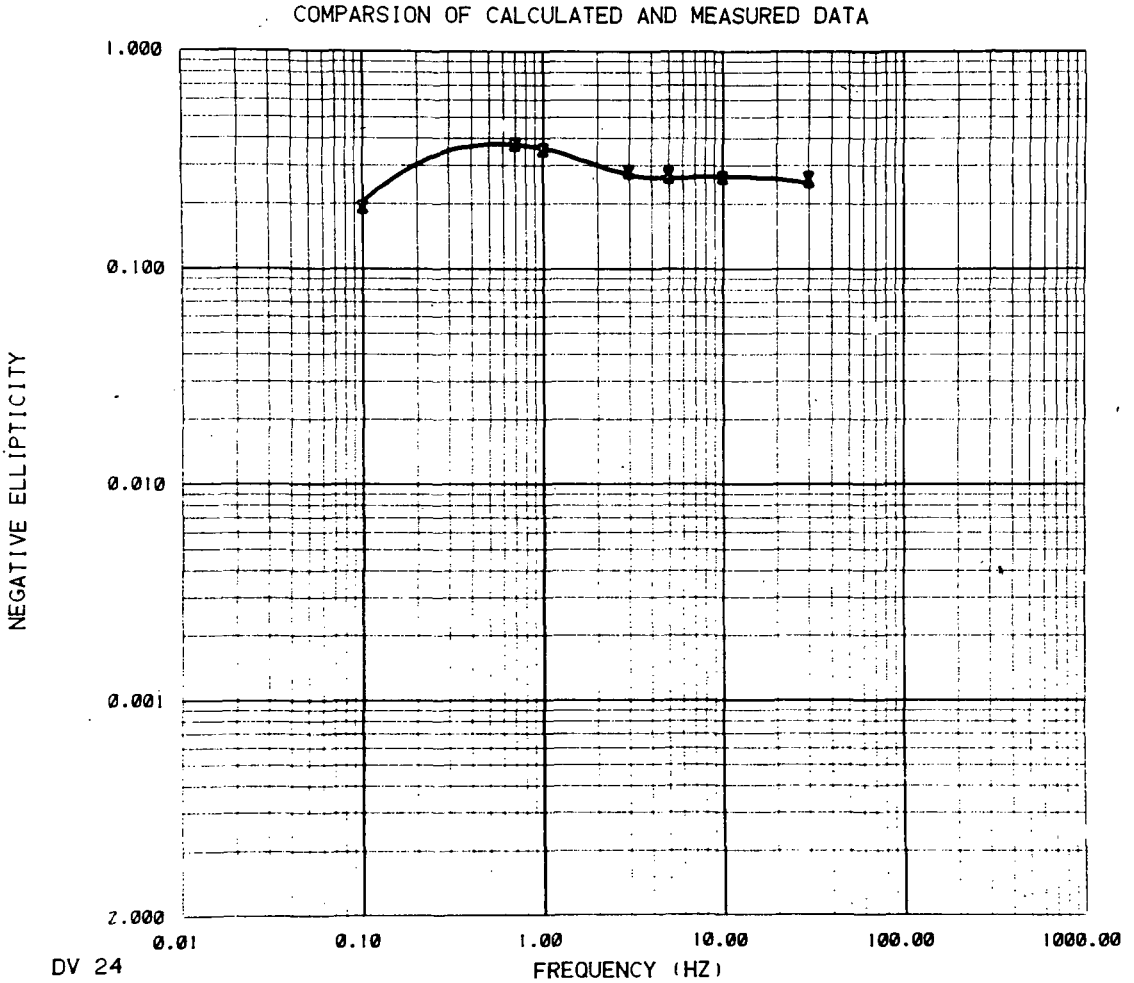

DV 24

CALCULATED DATA : MEASURED DATA

ELLIPTICITY ——— ELLIPTICITY

	LAYER	RESISTIVITY(OHM-M)		THICKNESS(M)	
X	1	11.89	± .8177E-02	416.5	± 23.
	2	1.529	± .1638	671.3	± 286.
	3	.8126E+07	± .3163E+14	.1000E+11	± 0.

DATA VARIENCE ESTIMATE .6331

XBL 829-11370

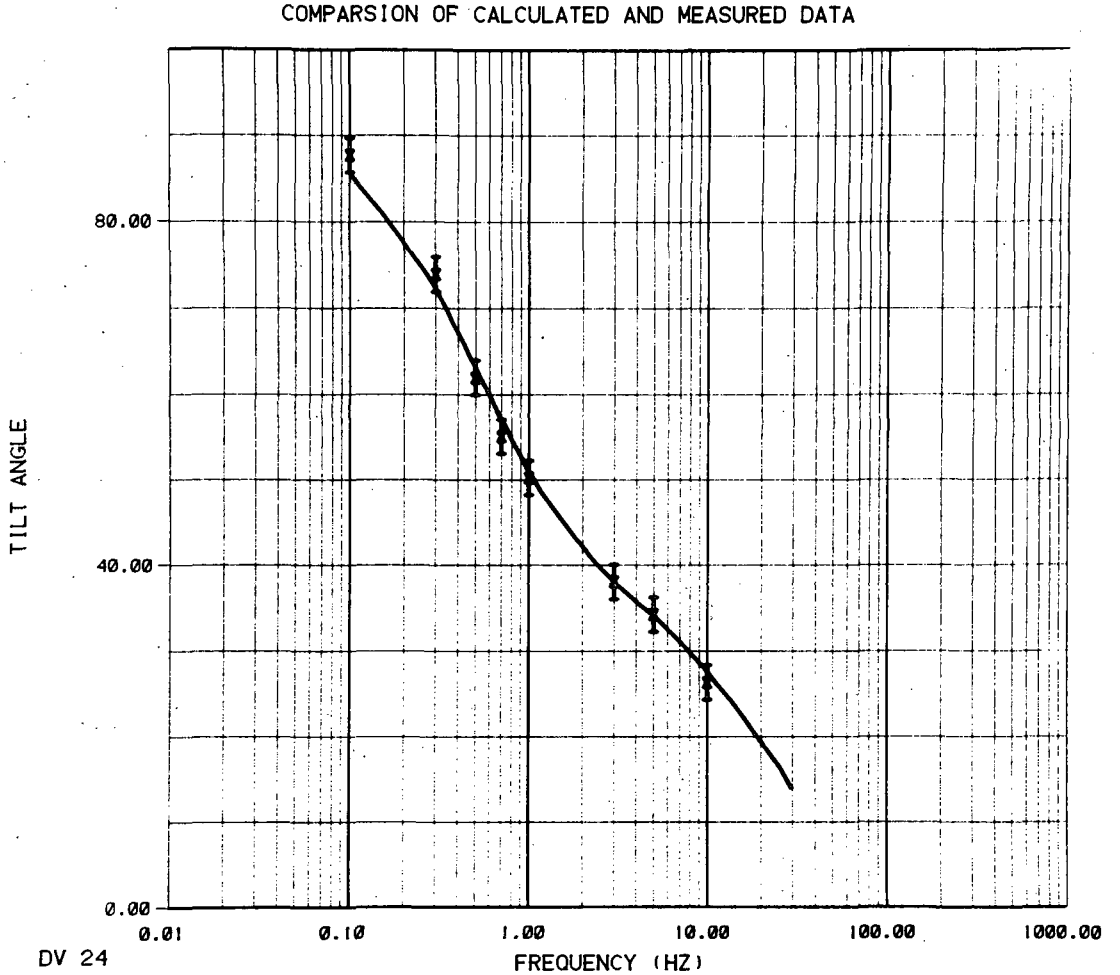

DV 24

CALCULATED DATA

TILT ANGLE ———

MEASURED DATA

TILT ANGLE X

LAYER	RESISTIVITY(OHM-M)	THICKNESS(M)
1	11.89 ± .8177E-02	416.5 ± 23.
2	1.529 ± .1638	671.3 ± 286.
3	.8126E+07 ± .3163E+14	.1000E+11 ± 0.

DATA VARIENCE ESTIMATE .6331

XBL 829-11371

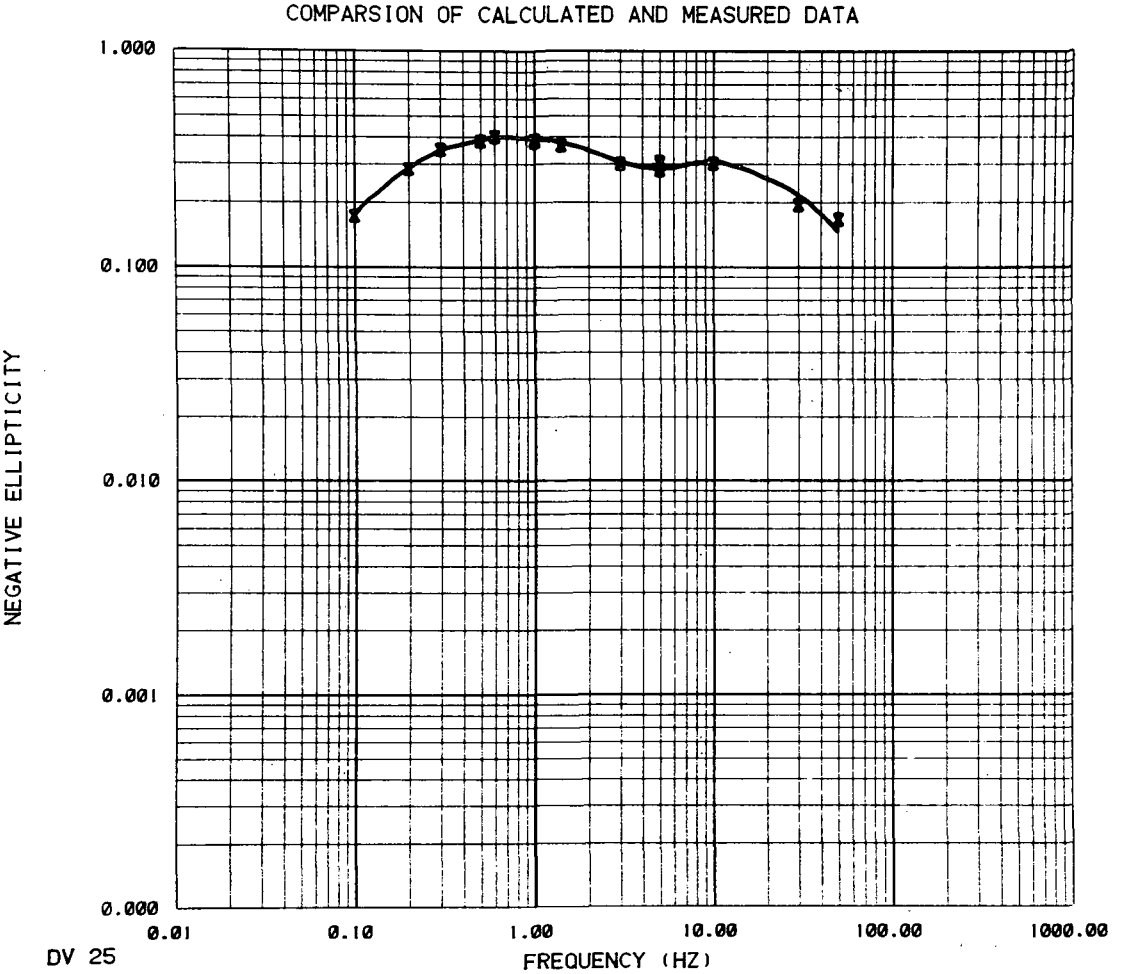

DV 25

CALCULATED DATA — ELLIPTICITY

MEASURED DATA — ELLIPTICITY

	LAYER	RESISTIVITY(OHM-M)		THICKNESS(M)	
X	1	13.65	± .6677E-02	582.8	± 53.
	2	2.014	± .5372	479.8	± 204.
	3	212.8	± 3195.	.1000E+11	± 0.

DATA VARIENCE ESTIMATE .9172

XBL 829-11362

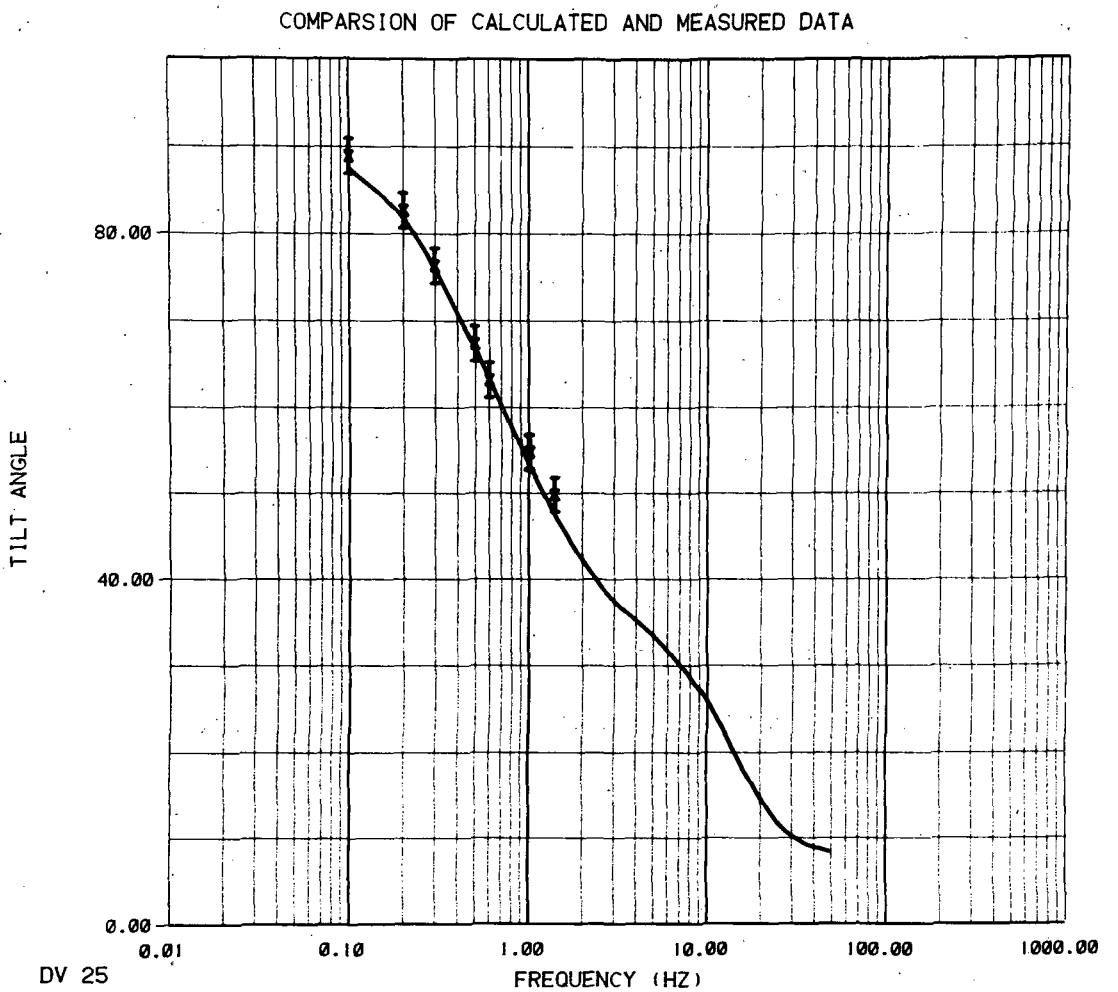

DV 25

CALCULATED DATA

TILT ANGLE ———— MEASURED DATA TILT ANGLE

	LAYER	RESISTIVITY(OHM-M)		THICKNESS(M)	
X	1	13.65	± .6677E-02	582.8	± 53.
	2	2.014	± .5372	479.8	± 204.
	3	212.8	± 3195.	.1000E+11	± 0.

DATA VARIENCE ESTIMATE .9172

XBL 829-11361

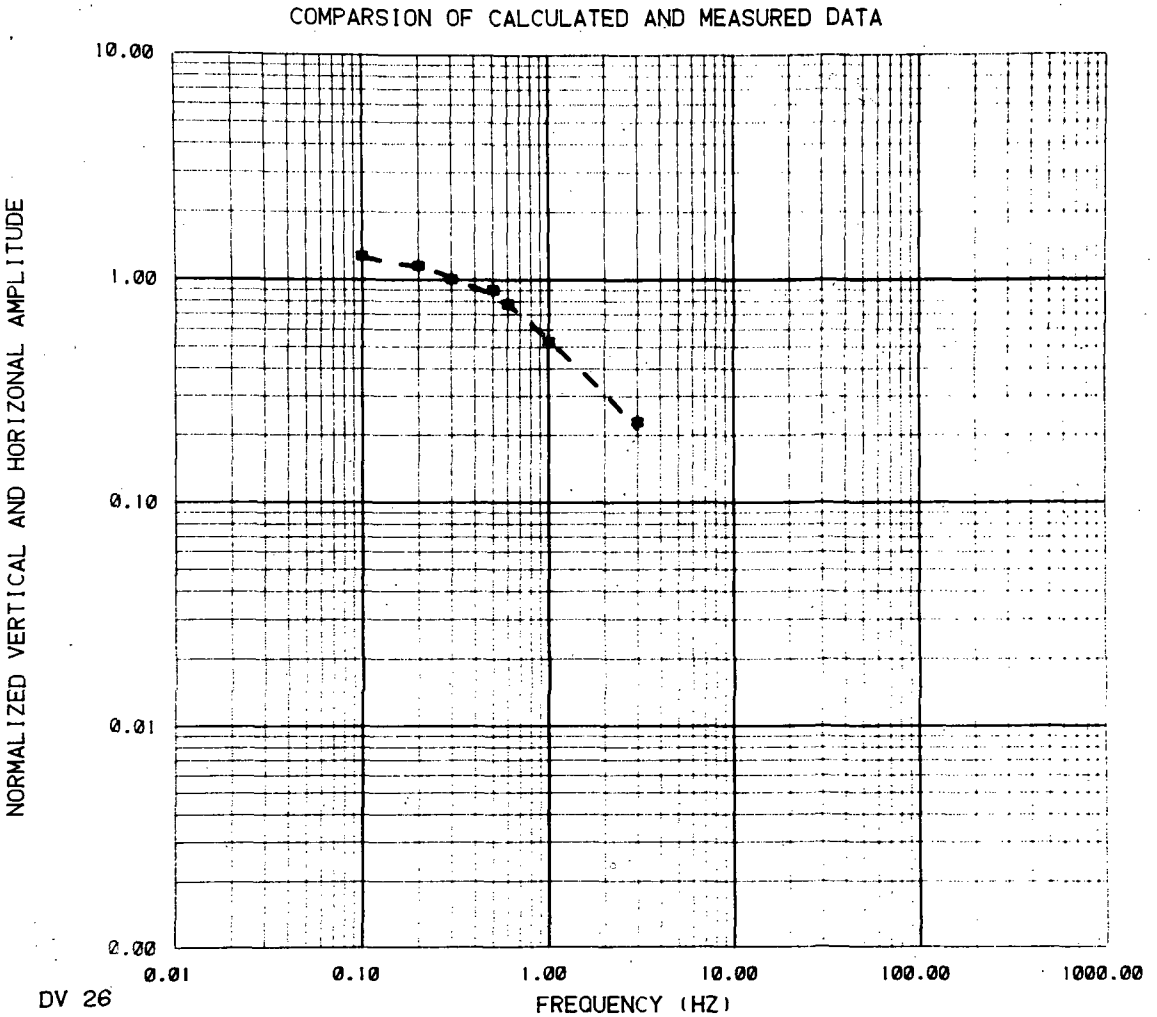

DV 26

CALCULATED DATA		MEASURED DATA		LAYER	RESISTIVITY(OHM-M)		THICKNESS(M)	
HR	———————	HR	X	1	6.725	± .2802E-02	688.5	± 30.
HZ	— — —	HZ	*	2	2.529	± .1324	1162.	± 92.
				3	.7888	± .1196	.1000E+11	± 0.

DATA VARIENCE ESTIMATE 17.05

XBL 829-11652

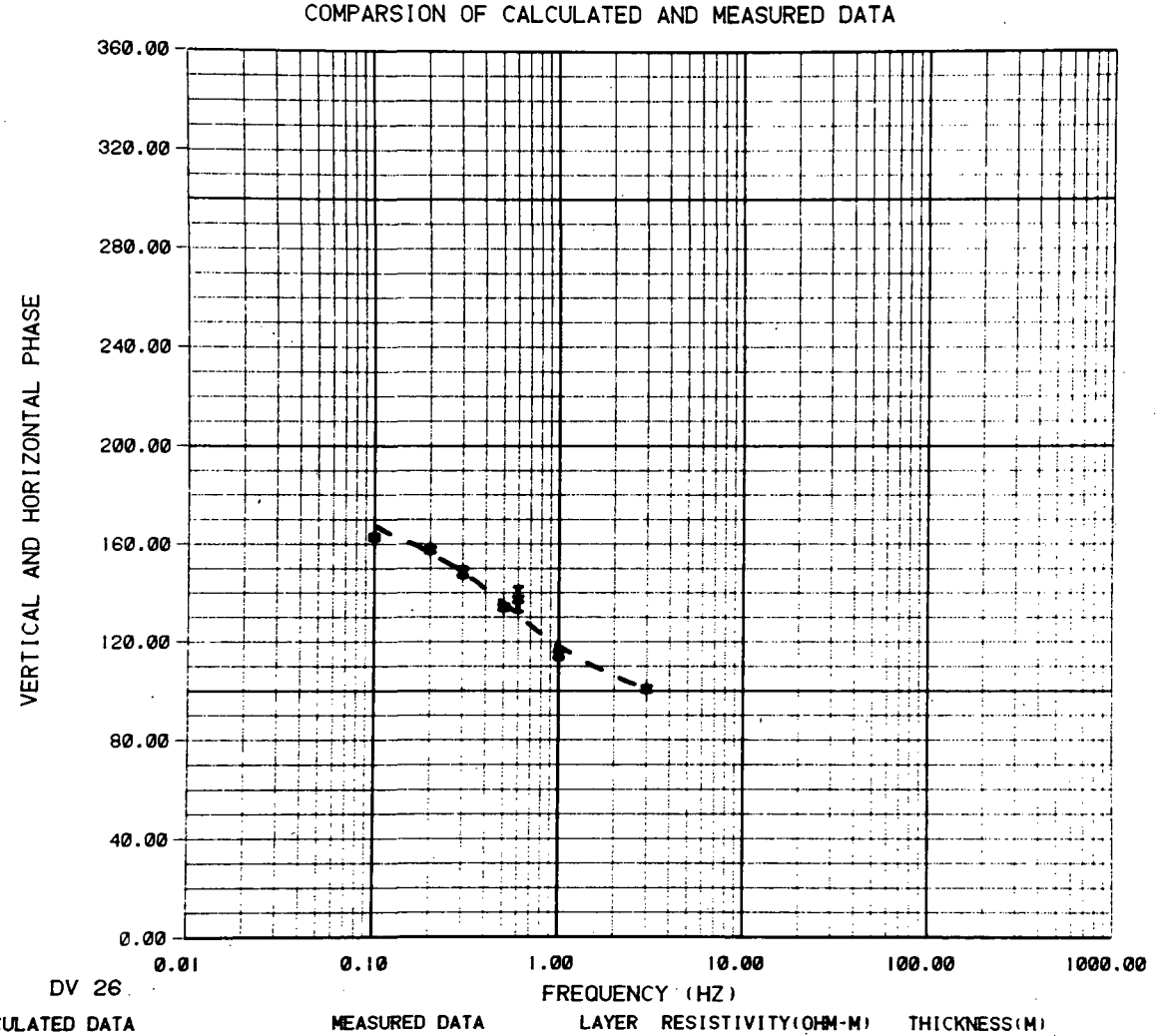

DV 26

CALCULATED DATA		MEASURED DATA		LAYER	RESISTIVITY(OHM-M)		THICKNESS(M)	
HR	———	HR	X	1	6.725	± .2802E-02	688.5	± 30.
HZ	— — —	HZ	*	2	2.529	± .1324	1162.	± 92.
				3	.7888	± .1196	.1000E+11	± 0.

DATA VARIENCE ESTIMATE 17.05

XBL 829-11651

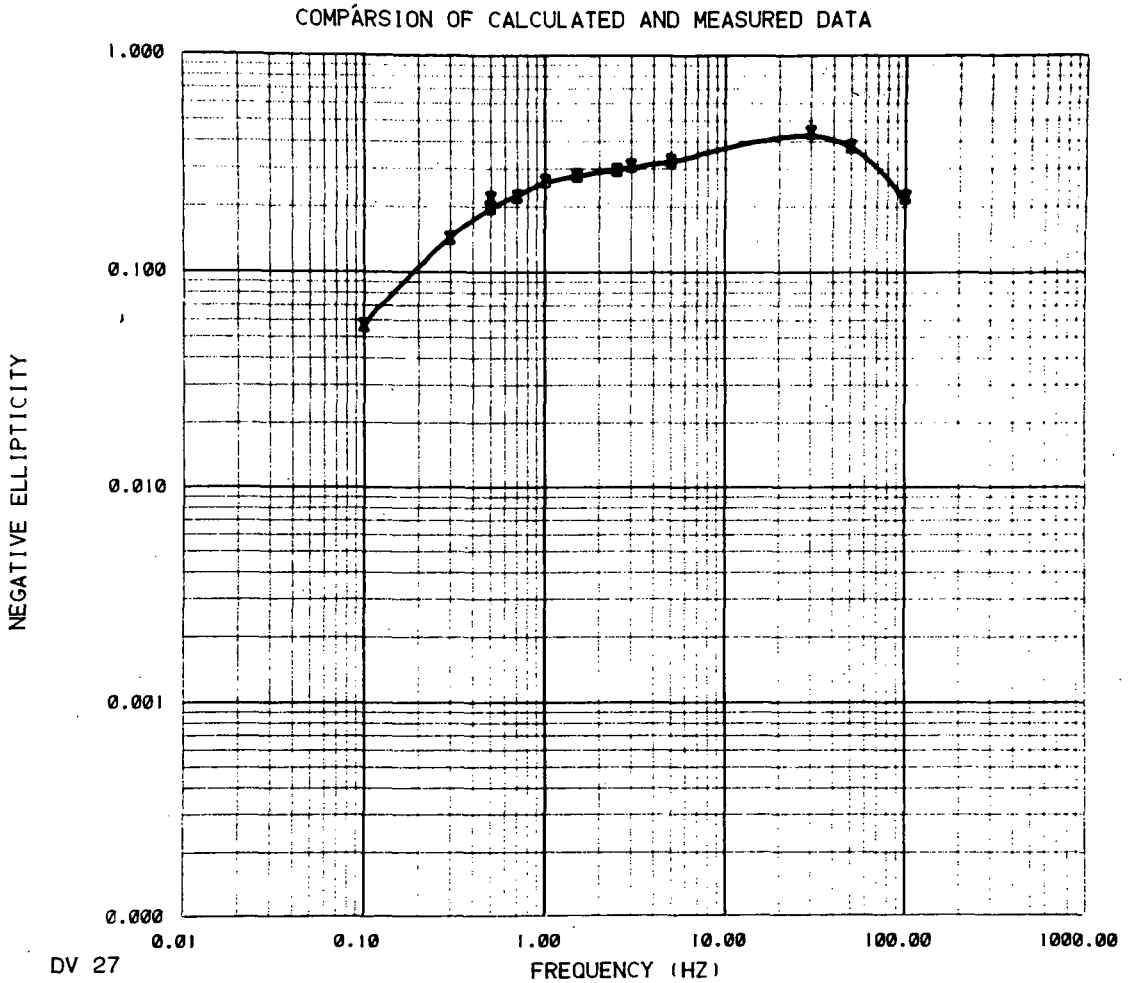

DV 27

CALCULATED DATA — ELLIPTICITY

MEASURED DATA — ELLIPTICITY

	LAYER	RESISTIVITY(OHM-M)		THICKNESS(M)	
X	1	23.78	± .4435E-02	687.3	± 55.
	2	3.638	± .9312	712.4	± 515.
	3	542.5	± .3853E+05	.1000E+11	± 0.

DATA VARIENCE ESTIMATE .6102

XBL 829-11368

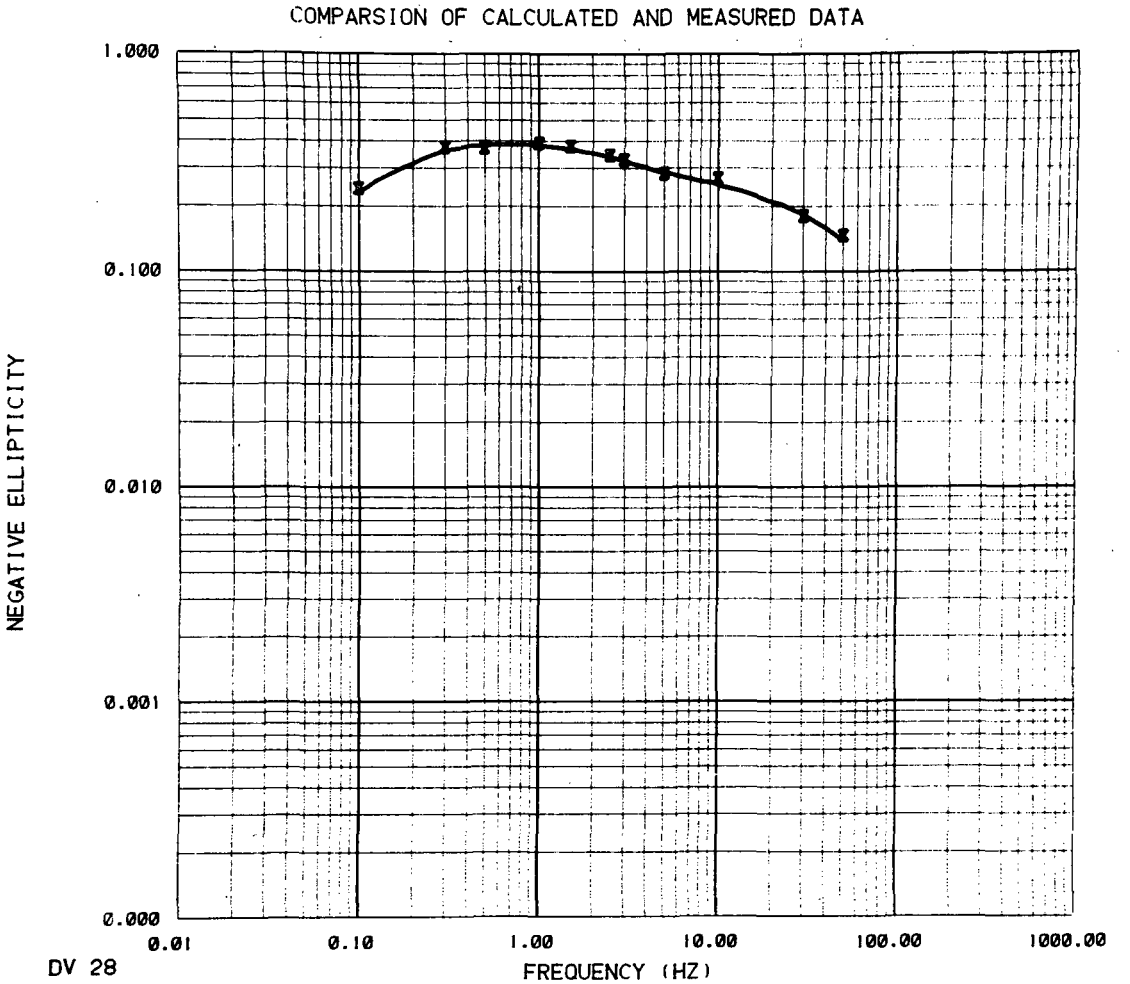

DV 28

CALCULATED DATA — ELLIPTICITY

MEASURED DATA — ELLIPTICITY

	LAYER	RESISTIVITY(OHM-M)		THICKNESS(M)	
X	1	7.805	± .9041E-02	325.9	± 21.
	2	1.993	± .1345	1292.	± 673.
	3	.1931E+09	± .2906E+17	.1000E+11	± 0.

DATA VARIENCE ESTIMATE .5435

XBL 829-11336

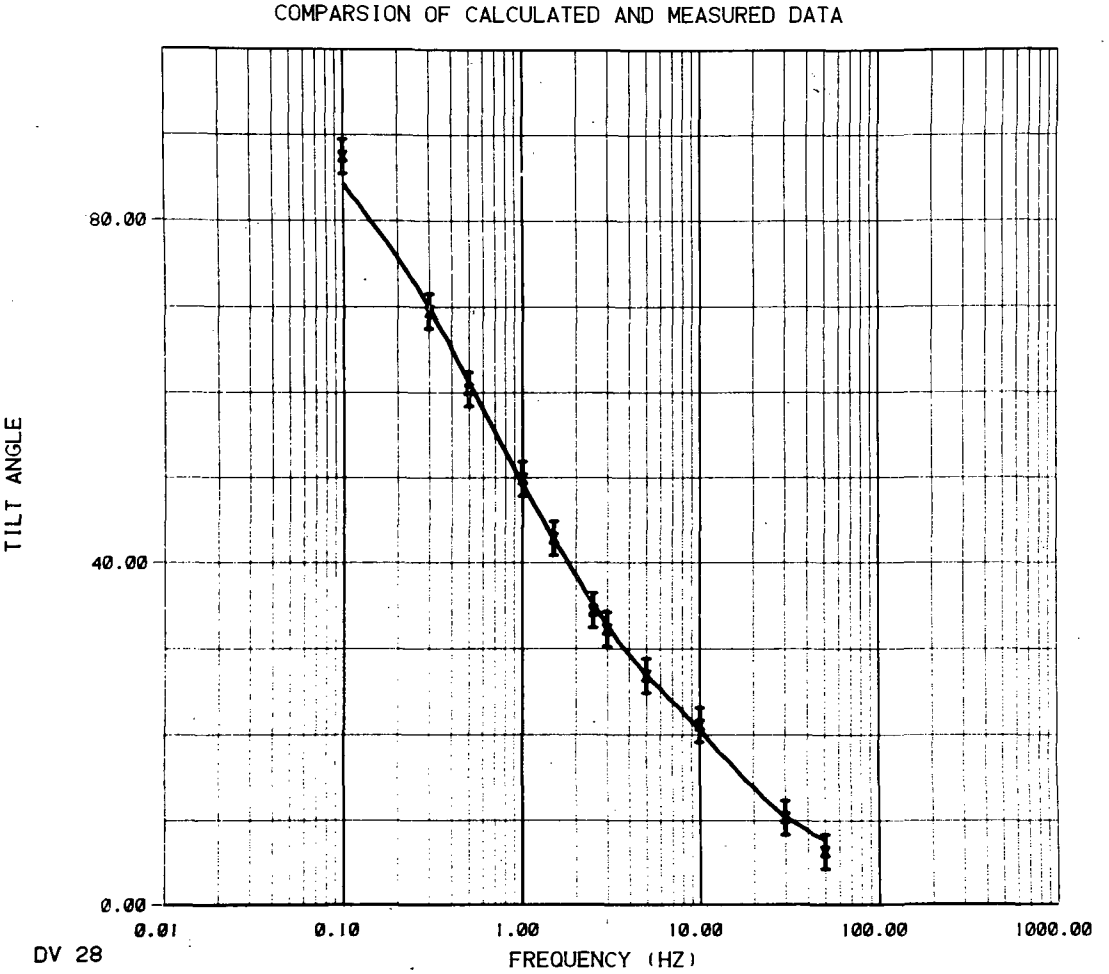

XBL 829-11335

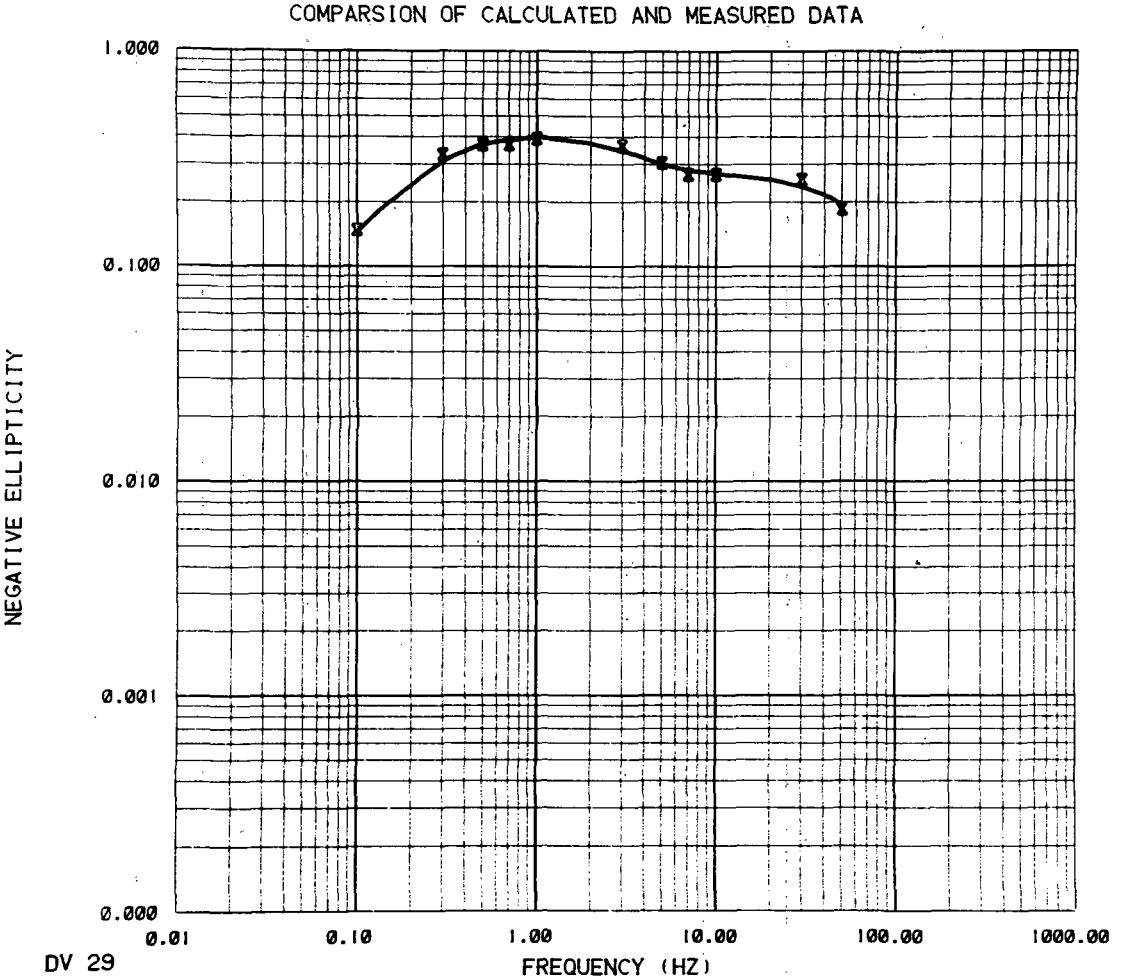

DV 29

CALCULATED DATA — ELLIPTICITY

MEASURED DATA — ELLIPTICITY

	LAYER	RESISTIVITY(OHM-M)		THICKNESS(M)	
X	1	20.32	± .6793E-02	432.2	± 27.
	2	4.241	± .3386	892.7	± 275.
	3	113.6	± 966.5	.1000E+11	± 0.

DATA VARIENCE ESTIMATE .7085

XBL 829-11367

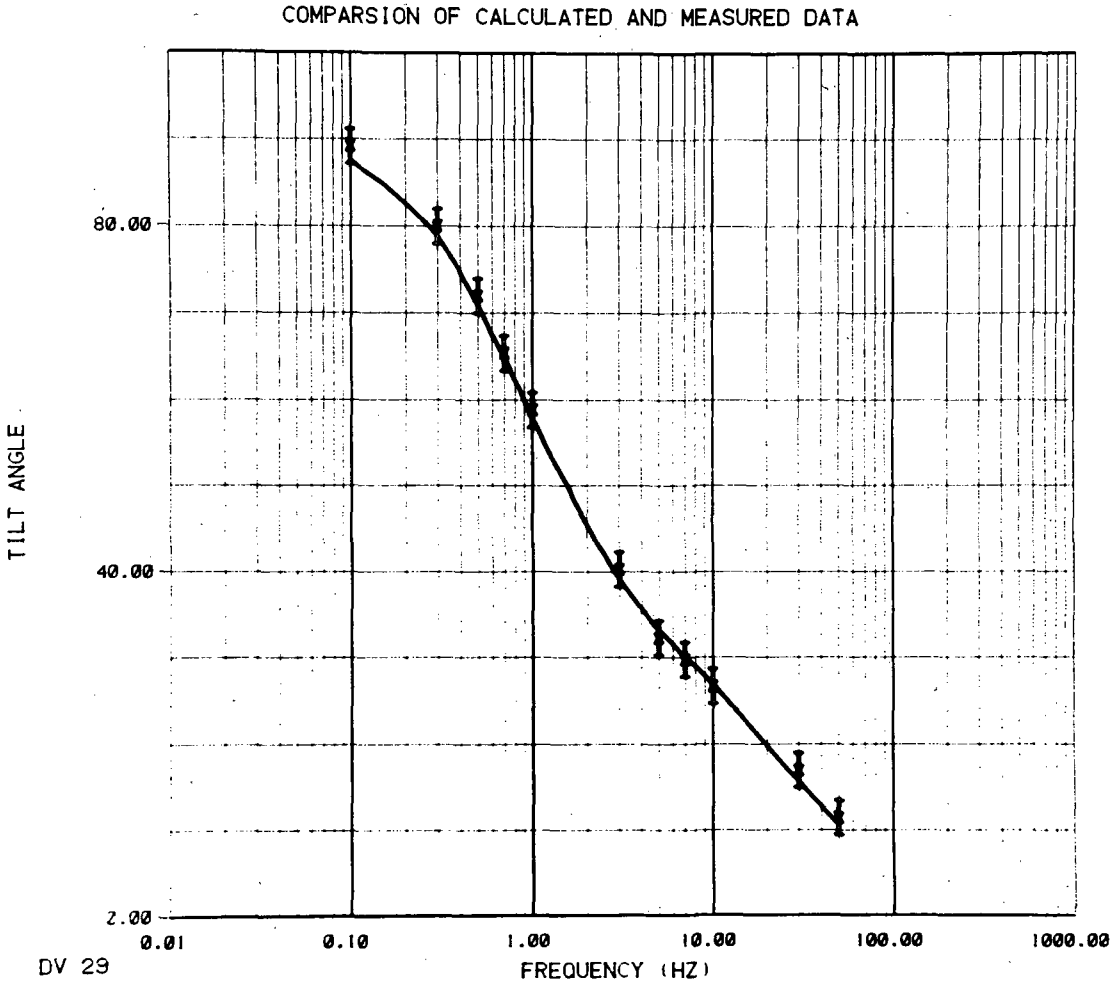

DV 29

CALCULATED DATA		MEASURED DATA		LAYER	RESISTIVITY(OHM-M)		THICKNESS(M)	
TILT ANGLE	———	TILT ANGLE	X	1	20.32	± .6793E-02	432.2	± 27.
				2	4.241	± .3386	892.7	± 275.
				3	113.6	± 966.5	.1000E+11	± 0.

DATA VARIENCE ESTIMATE .7085

XBL 829-11366

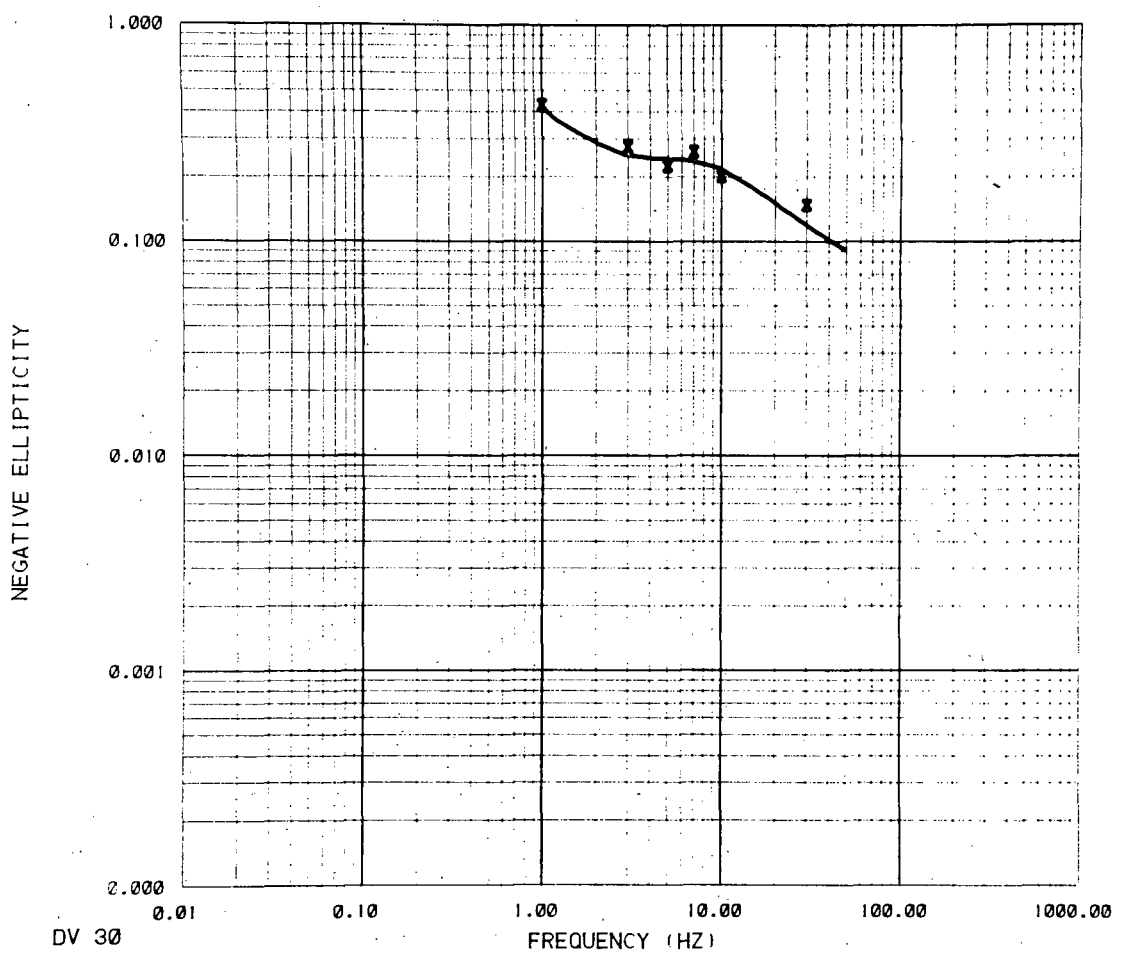

DV 30

CALCULATED DATA — ELLIPTICITY

MEASURED DATA — ELLIPTICITY

	LAYER	RESISTIVITY(OHM-M)		THICKNESS(M)	
X	1	13.81	± .2292E-01	677.6	± 70.
	2	3.158	± .9966	707.5	± 314.
	3	4300.	± .4580E+07	.1000E+11	± 0.

DATA VARIENCE ESTIMATE 4.539

XBL 829-11342

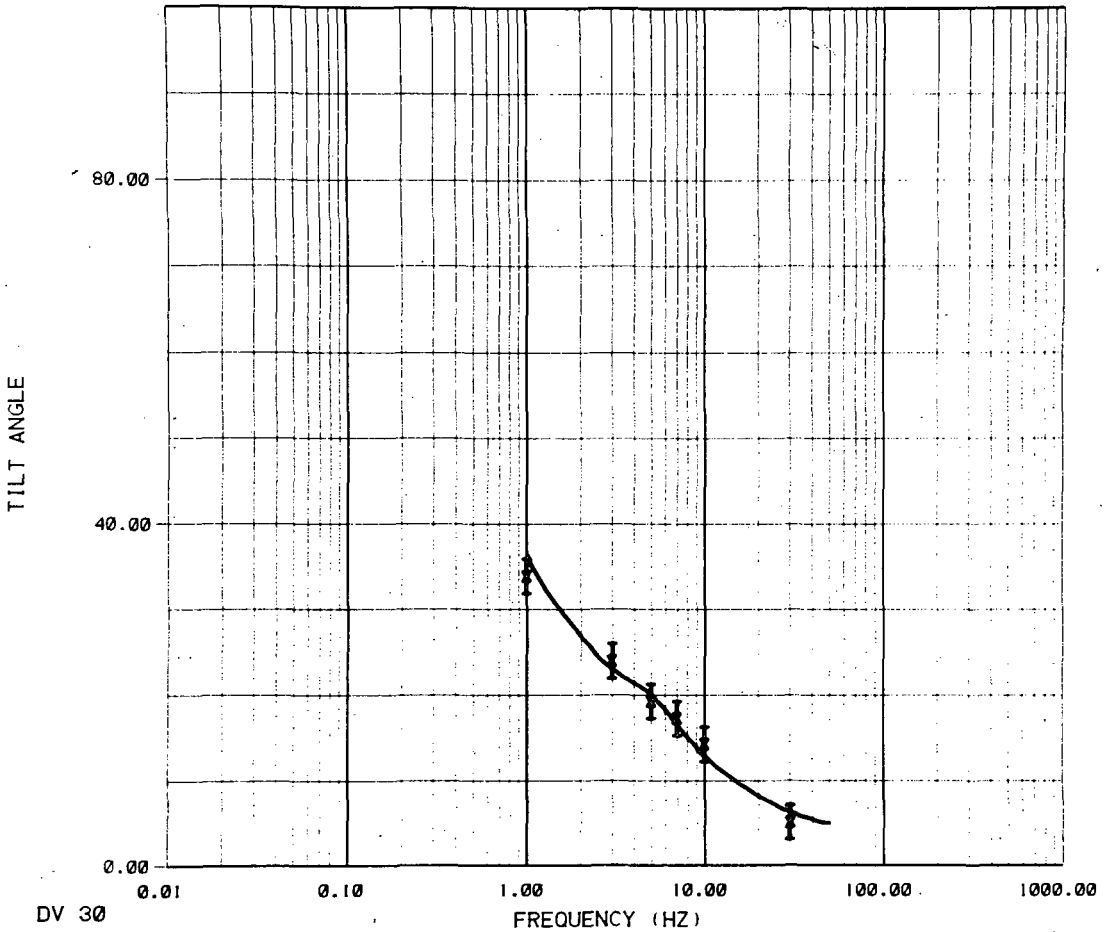

DV 30

CALCULATED DATA — MEASURED DATA

TILT ANGLE ——— TILT ANGLE

	LAYER	RESISTIVITY(OHM-M)		THICKNESS(M)	
X	1	13.81	± .2292E-01	677.6	± 70.
	2	3.158	± .9966	707.5	± 314.
	3	4300.	± .4580E+07	.1000E+11	± 0.

DATA VARIENCE ESTIMATE 4.539

XBL 829-11341

TECHNICAL INFORMATION DEPARTMENT
LAWRENCE BERKELEY LABORATORY
UNIVERSITY OF CALIFORNIA
BERKELEY, CALIFORNIA 94720